

# Large-scale structure and entrainment in the supersonic mixing layer

By N. T. CLEMENS† AND M. G. MUNGAL

High Temperature Gasdynamics Laboratory, Mechanical Engineering Department, Stanford University, Stanford, CA 94305, USA

(Received 10 August 1992 and in revised form 2 August 1994)

Experiments were conducted in a two-stream planar mixing layer at convective Mach numbers,  $M_c$ , of 0.28, 0.42, 0.50, 0.62 and 0.79. Planar laser Mie scattering (PLMS) from a condensed alcohol fog and planar laser-induced fluorescence (PLIF) of nitric oxide were used for flow visualization in the side, plan and end views. The PLIF signals were also used to characterize the turbulent mixture fraction fluctuations.

Visualizations using PLMS indicate a transition in the turbulent structure from quasi-two-dimensionality at low convective Mach number, to more random three-dimensionality for  $M_c \geq 0.62$ . A transition is also observed in the core and braid regions of the spanwise rollers as the convective Mach number increases from 0.28 to 0.62. A change in the entrainment mechanism with increasing compressibility is also indicated by signal intensity profiles and perspective views of the PLMS and PLIF images. These show that at  $M_c = 0.28$  the instantaneous mixture fraction field typically exhibits a gradient in the streamwise direction, but is more uniform in the cross-stream direction. At  $M_c = 0.62$  and 0.79, however, the mixture fraction field is more streamwise uniform and with a gradient in the cross-stream direction. This change in the composition of the structures is indicative of different entrainment motions at the different compressibility conditions. The statistical results are consistent with the qualitative observations and suggest that compressibility acts to reduce the magnitude of the mixture fraction fluctuations, particularly on the high-speed edge of the layer.

---

## 1. Introduction

The role of compressibility in turbulent mixing remains an important issue in the design of high-speed propulsion devices. Of particular interest are the free-shear flows such as mixing layers, jets and wakes, where the stabilizing effect of compressibility may reduce the efficiency of engines which utilize these flows to mix the fuel and oxidizer. The mixing layer is a particularly important flow for the study of compressibility because the free-stream conditions (and hence overall compressibility) remain constant with downstream distance. This is in contrast to the jet and the wake which evolve to incompressible flow behaviour with downstream distance.

Although not as well studied as its incompressible counterpart, the compressible mixing layer (figure 1) has been studied for several decades. Until recently, however, studies of supersonic mixing layers involved mainly time-averaged growth rate measurements, with fewer studies providing velocity or scalar fluctuation data. Birch & Eggers (1972) summarized the current growth rate data and showed a clear trend of reduced mixing layer growth rates with increasing Mach number. Bogdanoff (1983)

† Present address: Department of Aerospace Engineering and Engineering Mechanics, The University of Texas at Austin, Austin, TX 78712, USA.

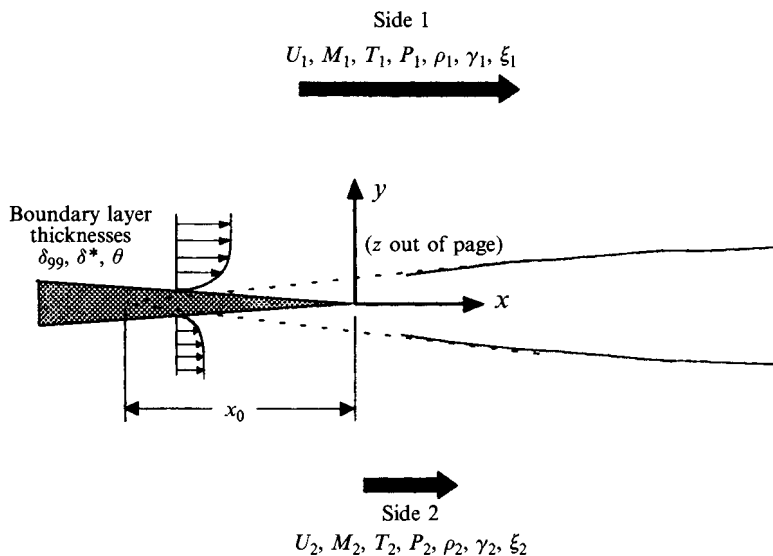


FIGURE 1. Schematic diagram of the mixing layer flow field.

and Papamoschou & Roshko (1988) generalized this result for both single- and two-stream mixing layers with the concept of the convective Mach number. In this paper, we will refer to the convective Mach number,  $M_c = (U_1 - U_2)/(a_1 + a_2)$ , which is the same as the Papamoschou & Roshko (1988) formulation for equal ratio of specific heats ( $U_1$  and  $U_2$ , and  $a_1$  and  $a_2$ , are the high- and low-speed free-stream velocities and speeds of sound, respectively).

Studies have shown that in addition to decreasing mixing layer growth rates, compressibility acts to suppress turbulence intensities and Reynolds stresses (Ikawa & Kubota 1975; Elliott & Samimy 1990; Goebel & Dutton 1991). Numerical studies using both linear stability theory and direct simulations have shown that at low compressibility ( $M_c < 0.6$ ) the structure is dominated by the two-dimensional Kelvin-Helmholtz instability, while at higher levels of compressibility, the dominant instability waves are oblique (Ragab & Wu 1989; Jackson & Grosch 1989; Zhuang, Dimotakis & Kubota 1990), resulting in highly three-dimensional structure in the non-linear regime (Sandham & Reynolds 1991).

Several experiments using both flow visualization and fast response pressure measurements have shown that low convective Mach number supersonic mixing layers exhibit an organized quasi-two-dimensional structure similar to that found in incompressible mixing layers (Clemens & Mungal 1992*a*; Messersmith, Dutton & Krier 1991; Shau & Dolling 1992; Elliott, Samimy & Arnette 1993; Petullo & Dolling 1993). The trend of decreasing organization or increased three-dimensionality with increasing convective Mach number has also been observed by a number of investigators (Fourquette, Mungal & Dibble 1990; Clemens & Mungal 1992*a*; Messersmith *et al.* 1991; Samimy, Reeder & Elliott 1992; Elliott *et al.* 1993; Bonnet, Debisschop & Chambres 1993). Possibly related to the increased three-dimensionality of the compressible layer is the observation that the large-scale structures do not travel at the speed predicted by the convective Mach number formulation of Papamoschou & Roshko (1988) (Papamoschou 1991; Fourquette *et al.* 1990; McIntyre & Settles 1991; Hall, Dimotakis & Rosemann 1991*a*).

A few passive scalar mixing measurements have also been reported. Passive scalar

Study	Fluid	$Re_{\delta 1}$	$L/\lambda_B$	PDFs	Mean inflection point
Sunyach & Mathieu (1969)	Gas	50000	600	—	Single
Fiedler (1974)	Gas	100000	100	—	Triple
Batt (1977)	Gas	70000	100	Marching	Single
Konrad (1977)	Gas	40000	11	Non-marching	Triple
Rajagopalan & Antonia (1981)	Gas	35000	70	—	Triple
Koochesfahani & Dimotakis (1986)	Water	23000	700	Non-marching	Triple
Masutani & Bowman (1986)	Gas	3200	250	Non-marching	Triple

TABLE 1. Comparison of scalar measurement data

mixing measurements can in general be problematic, however, because the spatial and temporal resolution must be sufficient to resolve the smallest scalar fluctuations, otherwise the amount of mixed fluid will be overestimated. The smallest mixing scale is the Batchelor scale,  $\lambda_B = \beta \delta Re_{\delta}^{-3/4} Sc^{-1/2}$ , where  $\beta$  is a constant,  $\delta$  is the local layer width,  $Re_{\delta}$  is the local Reynolds number based on the velocity difference of the shear flow and  $\delta$ , and  $Sc = \nu/D$  is the Schmidt number, or the ratio of the kinematic viscosity to the mass diffusion coefficient. Dowling & Dimotakis (1990) made high-resolution measurements in jets and suggest  $\beta \approx 25$ . As a means of quantifying the resolution of an experiment, we will refer to the relative resolution,  $L/\lambda_B$ , where  $L$  is the largest dimension of the probe volume and  $\lambda_B$  is defined above with  $\beta = 1$ . The relative resolutions of several incompressible mixing layer experiments are shown in table 1 and will be discussed further in §5.

Passive scalar mixing measurements in supersonic mixing layers were made by Dutton *et al.* (1990) using Mie scattering from seeded particles, and Clemens *et al.* (1991), Messersmith & Dutton (1992) and Clemens & Paul (1993) using nitric oxide laser-induced fluorescence. These studies report probability density functions (PDFs) of mixture fraction whose peak value ‘marches’ with cross-stream direction across the layer. This result is in agreement with the incompressible mixing layer measurements of Batt (1977) and Karasso & Mungal (1992), but not with the results of Konrad (1977) and Koochesfahani & Dimotakis (1986), where the peak mixture fraction was found to be constant with cross-stream location. Dutton *et al.* (1990) and Clemens *et al.* (1991) also found that the fraction of mixed fluid within the layer increased from low to moderate convective Mach numbers. The measurements of Messersmith & Dutton (1992), which were made at similar convective Mach numbers, did not show a clear trend for the fraction of mixed fluid. The results of these studies should be interpreted with caution as the measurements were highly under-resolved ( $L/\lambda_B > 500$ ).

As a means of avoiding the problem of poor resolution in making mixing measurements, Hall, Dimotakis & Rosemann (1991*b*) made quantitative measurements of product formation using  $H_2$ - $F_2$ -NO chemistry in planar supersonic shear layers. They studied two convective Mach number cases ( $M_c = 0.51$  and  $0.96$ ) and determined that the fraction of mixed fluid was lower at the high convective Mach number condition, which is opposite to the trend observed by Dutton *et al.* (1990) and Clemens *et al.* (1991). Clemens & Paul (1993) used a fluorescence quenching technique that mimics a fast chemical reaction, and thus is highly insensitive to finite resolution. They found in axisymmetric mixing layers that the fraction of mixed fluid was virtually the same at convective Mach numbers of 0.35 and 0.82.

In the present study, the structure of low to moderately compressible mixing layers was investigated using extensive flow visualizations with planar laser Mie scattering

(PLMS) from a seeded alcohol fog. These visualizations are compared to those made using planar laser-induced fluorescence (PLIF) imaging of seeded nitric oxide. The PLIF images are also used to generate statistical quantities, such as mean profiles, root-mean-square (RMS) fluctuations and probability density functions of mixture fraction.

Section 2 provides a description of the experimental apparatus, run conditions and diagnostic techniques used. Section 3 provides some background and theoretical justification for the optical diagnostic techniques, and the experimental results are discussed in §§4 and 5. Section 6 provides an overall discussion of the results, with conclusions offered in §7. Limited PLMS visualizations of the turbulent structure at three convective Mach numbers can be found in Clemens & Mungal (1992*a*). Complete details on all aspects of this work are detailed in Clemens (1991).

## 2. Experimental apparatus and run conditions

In this section the experimental facility, diagnostics set-up and experimental run conditions are discussed.

### 2.1. Wind tunnel

A schematic diagram of the flow system is shown in figure 2. The high-speed stream was supplied by a 6.9 MPa, 5 m<sup>3</sup> vessel, while the low-speed side was supplied by a 3.4 MPa, 2.5 m<sup>3</sup> vessel. A compressor delivered filtered and dried air to both tanks, and the two main flows were controlled using globe valves combined with microprocessor-based controllers. Maximum run times were 30–60 s, depending on the condition, with typical run times being 10–20 s.

The wind tunnel consisted of the plenum sections, nozzles, test section and diffuser. The tunnel was rectangular in cross-section with a width of 10 cm that remained constant over its entire length of about 180 cm. The high- and low-speed plenum sections (figure 3) were each 12 cm high, 10 cm wide and 55 cm and 85 cm long, respectively. The high-speed-side plenum had one station of honeycomb with a 0.8 mm cell size and 5 cm in length. The low-speed plenum contained two perforated plates of 55% porosity followed by two stations of honeycomb identical to that on the high-speed side. Stagnation pressures were measured using static pressure taps located on the sidewalls of each plenum. The high- and low-speed flows then passed through contractions of 9:1 and 4:1, respectively. The nozzle design was similar to that of Papamoschou & Roshko (1988) where a centre-body contained both the supersonic and subsonic contours. The supersonic contours were designed using a closed form solution to the method of characteristics (Foelsch 1946) and the subsonic contour of the centre-body followed a fifth-order polynomial. Three aluminium nozzles were used with design exit Mach numbers of 1.5, 2.0 and 2.2.

The high-speed nozzle exit height ( $y$  dimension) was 2.5 cm for all three nozzles. The low-speed nozzle exit height was either 3 cm or 4.5 cm depending on the particular convective Mach number condition: the 3 cm height for the lowest convective Mach number case and the 4.5 cm height for the higher Mach number cases. The differing heights were used to accommodate the differing rates of mixing layer growth. The test section length ( $x$  dimension) was 48 cm and 10 cm in width ( $z$  dimension). For variation of the streamwise pressure gradient, the top and bottom walls were adjustable using a thin flexible member design similar to that of Papamoschou & Roshko (1988). Optical access was provided through the sides from  $-0.5$  cm to 45 cm from the splitter tip, and through the top and bottom from 15 cm to 45 cm. The windows were constructed of acrylic for all runs except for the PLIF experiments where smaller fused silica windows were used. The windows were carefully mounted so as to minimize the

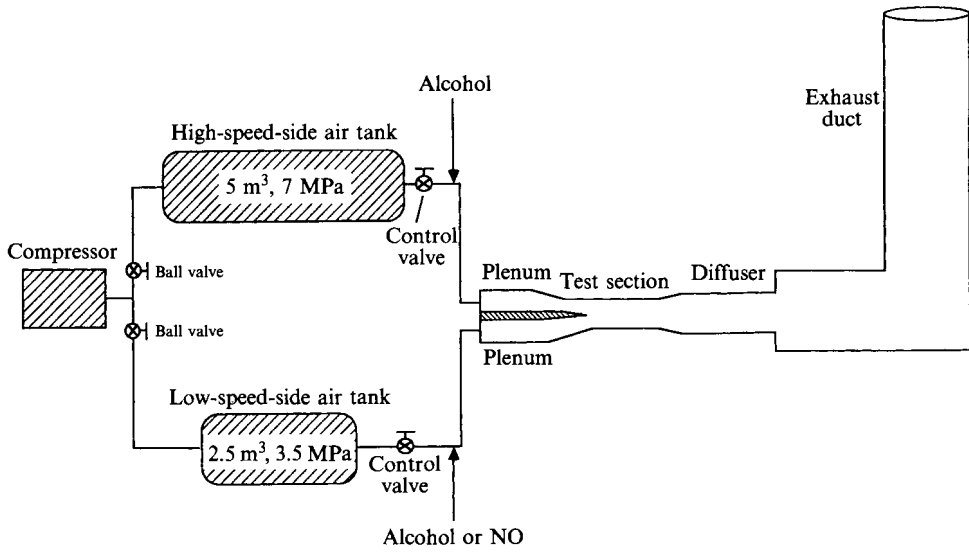


FIGURE 2. Simplified diagram of the gas supply system.

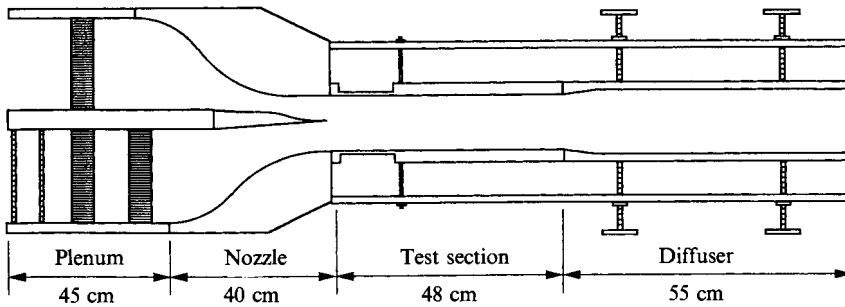


FIGURE 3. Diagram of the wind tunnel showing the plenum sections, nozzles, and the test and diffuser sections. The figure is not to scale.

Case	$M_c = 0.28$	$M_c = 0.42$	$M_c = 0.50$	$M_c = 0.62$	$M_c = 0.79$
Gas <sub>1</sub> , Gas <sub>2</sub>	Air, air	Air, air	Air, air	Air, air	Air, argon
$M_1, M_2$	1.64, 0.91	1.52, 0.51	1.50, 0.38	2.0, 0.40	2.2, 0.39
$U_1, U_2$ (m s <sup>-1</sup> )	430, 275	416, 165	413, 118	480, 130	508, 110
$T_{01}, T_{02}$ (K)	265, 260	270, 271	271, 259	265, 260	265, 260
$T_1, T_2$ (K)	172, 223	187, 260	188, 252	150, 252	140, 253
$P_{01}, P_{02}$ (kPa)	302, 115	310, 100	265, 80	495, 75	600, 67
$\dot{m}_1, \dot{m}_2$ (kg s <sup>-1</sup> )	1.6, 0.77	1.5, 0.53	1.3, 0.51	1.8, 0.37	1.84, 0.39
$U_1/\nu_1, U_2/\nu_2$ (cm <sup>-1</sup> × 10 <sup>-5</sup> )	4.8, 1.9	5.0, 1.1	4.3, 0.75	6.5, 0.74	7.0, 0.55
Density ratio, $s$	0.77	0.72	0.75	0.59	0.77
Velocity ratio, $r$	0.63	0.40	0.29	0.27	0.22
$(\omega_{alc})_1, (\omega_{alc})_2$	0.002, 0.004	—, 7.6	2.1, 6.6	0.002, 0.008	0.0016, 0.008
$(\chi_{No})_2$ (p.p.m.)	1700	—	—	3500	—

TABLE 2. Run conditions

mismatch between the window and the frame. The importance of removing such discontinuities was demonstrated by Clemens & Mungal (1992*b*), who showed that through the generation of shock waves, sidewall discontinuities can significantly perturb supersonic mixing layers. Eight 0.8 mm diameter static pressure taps, with a separation of about 5 cm, were located on the top and bottom walls of the test section. After exiting the test section, the flow entered a straight duct supersonic diffuser and then exited to the atmosphere through an exhaust duct 50 cm diameter by 10 m long.

## 2.2. Diagnostics

The principal diagnostics used for this study were Pitot pressures, schlieren photography, PLMS visualization and PLIF. The Pitot probes were used to obtain the overall growth rate of the mixing layer while the schlieren and PLMS images were used for identification of the turbulent structure. The PLIF allowed further visualizations as well as the ability to make quantitative determinations of scalar transport. In addition to the imaging measurement, stagnation temperatures and static pressures were recorded as facility diagnostics. A 16 channel pressure scanner (Pressure Systems Inc.) was used to monitor the pressures throughout the test and diffuser sections.

The Pitot probes were constructed of 18 gauge (1.3 mm outer diameter) hypodermic needles of varying lengths, soldered to a stainless steel strut 1.6 mm thick by 2.54 cm wide (in the streamwise direction). The probe was moved vertically through the flow using a computer-controlled stepping motor with each trace consisting of about 30 points acquired in about 10 s.

The schlieren system was composed of a Xenon Nanolamp with a 20 ns pulse width, 30 cm diameter F/6 parabolic mirrors, 30 cm by 10 cm flat mirrors, a razor blade knife edge, and a CCD video camera (Pulnix TM540) with a telephoto lens as the imaging device.

The condensation fog methods involved the seeding of ethanol liquid into the low- or high-speed streams using an atomizing spray nozzle. The injection points were located approximately 5 m upstream of the test section providing enough time for the droplets to fully evaporate and become uniformly mixed before reaching the test section. The mass fractions of seeded ethanol vapour,  $\omega_{alc}$ , were from 0.002 to 0.008, with the actual values given in table 2.

For the PLMS visualizations, the laser used was a frequency-doubled Nd:YAG laser (Quantel 660B), with a 6 ns pulse width, pulse energy of 150 mJ and a 10 Hz repetition rate. The laser was formed into a sheet that was typically 15 cm wide and 300  $\mu\text{m}$  thick at the waist. The detector was a standard CCD video camera (Pulnix TM540) whose output was acquired using a Data Translation 2851 frame grabber installed in an IBM AT compatible computer equipped with 10 Mbytes of extended memory. The images were stored using the extended memory where a maximum of 80 images of 512  $\times$  240 resolution could be acquired at a rate of about 3 Hz.

For the PLIF studies, the  $A \leftarrow X(0,0) Q_1(J = 10.5)$  transition of nitric oxide (NO) was excited with laser light of wavelength 226.159 nm. The laser source was a XeCl (Lambda Physik EMG 160) pumped dye laser (Lambda Physik FL 3002) frequency doubled in BBO. The UV laser pulse width was about 20 ns with a spectral width of about 0.45  $\text{cm}^{-1}$ . The sheet was typically 6–7 cm wide and about 250–350  $\mu\text{m}$  thick at the waist. The camera system was an image-intensified CCD video camera (Amperex), of 512  $\times$  240 resolution, coupled to an F/1.2,  $f = 95$  mm Casagrainian reflective lens. The imaged region was about 5 cm, thus the nominal resolution was about 125  $\times$  200  $\times$  300  $\mu\text{m}$ , for the streamwise ( $x$ ), cross-stream ( $y$ ) and spanwise ( $z$ ) directions (figure 1), where the spanwise resolution is given by the sheet thickness. The actual

spatial resolution was worse than this, however, owing to filtering by the frame grabber, and the lens and image intensifier response characteristics. Paul (1991) discusses the resolution of the camera system used in the present study and concludes the resolution is further degraded by a factor of about 1.7, resulting in an actual resolution of about  $400 \times 400 \times 300 \mu\text{m}$ . We note, however, that owing to the low signal-to-noise ratios of the measurements, the resolution is actually approximately a factor of two worse than this (see §5).

The nitric oxide delivery system consisted of a bottle of pure NO which was located outside the building and brought into the laboratory through a 1.3 cm stainless steel line pressurized to 340 kPa and metered using a precision needle valve. The NO was seeded into the low-speed stream far enough upstream of the test section for it to become uniformly mixed.

### 2.3. Run conditions

Results will be presented for five convective Mach numbers: 0.28, 0.42, 0.50, 0.62 and 0.79. The different convective Mach number cases were achieved by varying the supersonic and subsonic Mach numbers and the low-speed gas molecular weight, with the specific conditions given in table 2. For all but the lowest convective Mach number case, the test section upper wall was kept level while the lower wall was converged about  $0.5^\circ$  in order to obtain a constant streamwise pressure distribution. For the  $M_c = 0.28$  case, however, both the upper and lower walls were diverged about  $0.5^\circ$ . This had the effect of accelerating both free streams to higher Mach numbers, such that the resulting convective Mach number was reduced significantly from its non-accelerated value.

Splitter plate boundary layer thicknesses were calculated using STAN7, a turbulent boundary layer code (Crawford & Kays 1976). The high-speed nozzle exit momentum thickness Reynolds numbers,  $Re_\theta = U_1 \theta_1 / \nu_1$ , were calculated to be  $7.2 \times 10^3$ ,  $10^4$ , and  $1.1 \times 10^4$  for the  $M_1 = 1.5$ , 2.0 and 2.2 nozzles, respectively. For Reynolds numbers of this magnitude, the boundary layers are expected to be turbulent. The calculated high-speed boundary layer thicknesses,  $\delta_{99}$ , at the nozzle exit, are 1.6, 1.5 and 1.6 mm, while the momentum thicknesses are,  $\theta_1 = 0.15$ , 0.14 and 0.12 mm, for the  $M_1 = 1.5$ , 2.0 and 2.2 nozzles, respectively. For the low-speed side,  $\delta_{99}$  boundary layer thicknesses were typically 1.0–1.5 mm. The calculations of the high-speed-side boundary layer thicknesses,  $\delta_{99}$ , agree well with the thicknesses of about 1.5 mm scaled from close-up schlieren photographs.

## 3. Diagnostic techniques

This section provides background information and theory for the PLMS and PLIF diagnostics.

### 3.1. Planar laser Mie scattering

The primary flow visualization method used in this study was planar laser Mie scattering from droplets that were formed from the condensation of seeded alcohol vapour. The condensation occurred in one of two modes, depending on whether the high- or low-speed stream was seeded. When the vapour was seeded into the low-speed stream, condensation would occur from the mixing of the low-speed fluid with the cold (140–180 K) high-speed fluid. Condensation, therefore, occurred only upon the molecular mixing of high- and low-speed fluid, and in this way, mimics product formation of a finite-rate chemical reaction (Masutani & Bowman 1986; Mungal & Frieler 1988). For this reason, we call this the ‘product formation’ method, in analogy to combustion systems. Alternatively, when the alcohol vapour was seeded into the

high-speed stream, the vapour condensed within the supersonic nozzle forming a fairly uniform marker of high-speed fluid (McGregor 1961). This method is analogous to passive scalar visualizations that have been used in incompressible mixing layers (Batt 1977; Breidenthal 1981; Masutani & Bowman 1986), thus we call it the 'passive scalar' method. Owing to droplet growth and evaporation, the scattering signals for the product formation and passive scalar methods are not strictly proportional to either the concentration of product or of high-speed fluid, respectively, as will be discussed below.

The condensation fog methods are discussed in detail in Clemens & Mungal (1991), and some of their most relevant results will be summarized here. The alcohol droplets were measured to have a mean diameter of less than  $0.2 \mu\text{m}$ , which is small enough to satisfy the Samimy & Lele (1991) criterion for correct visualizations of the large-scale turbulent structure. The number densities are large enough ( $> 10^9 \text{ cm}^{-3}$ ) that the droplets are expected to coagulate as they travel downstream, thus potentially affecting the scattering signal. Such coagulation, however, will cause a relatively gradual signal change and is not expected to affect the visualization of the turbulent motions. For certain mixture fractions, droplet re-evaporation is also expected to occur. This is particularly a problem with the passive scalar method when the high-speed fluid (which carries the droplets) becomes sufficiently diluted with the relatively warm low-speed fluid. This effect is expected to be largest for the low convective Mach number case, but even for this case, most of the mixed fluid should be visualized.

The time for complete condensation of ethanol vapour in a supersonic nozzle was measured by Wegener, Clumpner & Wu (1972) to be approximately  $50 \mu\text{s}$ , which we will use as an order of magnitude estimate for the 'chemical time' with the product formation method. This time is slow enough that finite rate effects should be evident, since this is of the same order as the local large-scale time,  $\delta/\Delta U$  ( $x = 30 \text{ cm}$ ), for all of the cases. It is believed, however, that conclusions concerning the large-scale structure of the flow are not compromised by finite rate effects for any of the convective Mach number cases. This is because no change in the turbulent structure is observed for a factor of three change in fluid timescales, or from  $x = 15 \text{ cm}$  until the end of the test section at  $x = 45 \text{ cm}$ .

### 3.2. Planar laser-induced fluorescence

Laser-induced fluorescence measurements can in general be difficult to interpret because the signal depends on the temperature, pressure, and the mole fractions of all species which collide with the fluorescent species. A simple fluorescence model can be used to obtain a relation between the fluorescence signal,  $S_f$ , and the flow field variables (Hanson, Seitzman & Paul 1990),

$$S_f \propto \chi_{NO} N(P, T) f_B(T) E_L \frac{1}{1 + Q_{el}/A}, \quad (1)$$

where  $\chi_{NO}$  is the mole fraction of NO,  $N$  is the total number density,  $f_B$  is the Boltzmann fraction,  $E_L$  is the laser energy,  $A$  is the spontaneous emission rate (which is constant), and  $Q_{el}$  is the electronic quenching rate, or the rate at which excited state molecules are de-excited through collisions. In the present experiments, where the NO is seeded into air and mixes only with air, we find that  $Q_{el} \propto NT^{1/2}$  and  $Q_{el} \gg A$ . Equation (1) then reduces to

$$S_f \propto \chi_{NO} \frac{f_B(T)}{T^{1/2}} E_L. \quad (2)$$

The Boltzmann fraction is determined by the ground-state energy level that is pumped, and a level can be chosen such that  $f_B \propto T^{1/2}$  over the temperature range of interest. Equation (2) then reduces to the relation  $S_f \propto \chi_{NO}$ , showing that the fluorescence signal is proportional to the NO mole fraction and is independent of pressure and temperature. The NO mole fraction is a conserved scalar, and upon normalization of the signal by its free-stream value we can define the mixture fraction,  $\xi$ , as

$$\xi = 1 - \chi_{NO}/(\chi_{NO})_2, \quad (3)$$

where the subscript 2 is used since, for all cases, the NO was seeded into the low-speed stream. The mixture fraction,  $\xi$ , represents the mass (or mole) fraction of high-speed fluid present within the probe volume. Clemens (1991) shows that the fluorescence signal is a linear function of mixture fraction to within 2–3%. It should be noted that the laser beam was noticeably absorbed (20–30%) on traversing the low-speed side of the layer, and all of the images were corrected for this using Beer's law.

#### 4. Experimental results: conventional measurements and PLMS imaging

This section describes the experimental results, first the conventional diagnostics and then PLMS visualizations. Note that not all of the diagnostics available were applied to each of the compressibility cases.

##### 4.1. Static and Pitot pressures

The test section static pressure distributions for all cases are shown in figure 4. As discussed previously, for the  $M_c = 0.28$  case, the flow was accelerated in order to obtain a lower convective Mach number. This is seen where the pressures on the high- and low-speed side are matched at the exits of both nozzles at about 80 kPa (corresponding to  $M_1 = 1.5$  and  $M_2 = 0.7$ ); the two flows then accelerate, reaching a uniform pressure of about 65 kPa from about 15–45 cm, where the pressures vary by less than 5% from the mean, with new free-stream Mach numbers of 1.64 and 0.91. The Pitot thickness growth rates were determined in this constant-pressure region. The pressures for the other cases remained constant to within about 20% throughout the test section.

Pitot traces for the three convective Mach number cases, 0.28, 0.62 and 0.79, are shown in figure 5 where the positions of each profile on the page are approximately to scale. The profiles for the  $M_c = 0.28$  case show that both free streams were relatively uniform throughout the entire test section. The bumps in the profiles are due to weak shocks and expansion waves which are also seen in the schlieren visualizations. Near the end of the test section the boundary layers on the top and bottom walls can be seen, and in all cases are less than about 7 mm thick. As with the static pressure distributions, stronger free-stream non-uniformity is seen at the higher convective Mach numbers. This non-uniformity is due to shock and expansion waves which diminish in strength with downstream distance.

In figure 6 the  $0.05\Delta P_{pit}$  and  $0.95\Delta P_{pit}$  points are plotted versus downstream distance for  $M_c = 0.28, 0.62$  and  $0.79$ , in order to show the growth and spatial location of the layers. The layers for all cases exhibit approximately linear growth in the downstream 2/3 of the test section where the effects of the initial shocks have largely dissipated.

The Pitot thickness,  $\delta_{pit}$ , was determined from the distance between the  $0.05\Delta P_{pit}$  and  $0.95\Delta P_{pit}$  points and when plotted versus downstream distance, the slope gives the growth rate, while the  $x$ -intercept gives the virtual origin,  $x_0$ . The slope was obtained

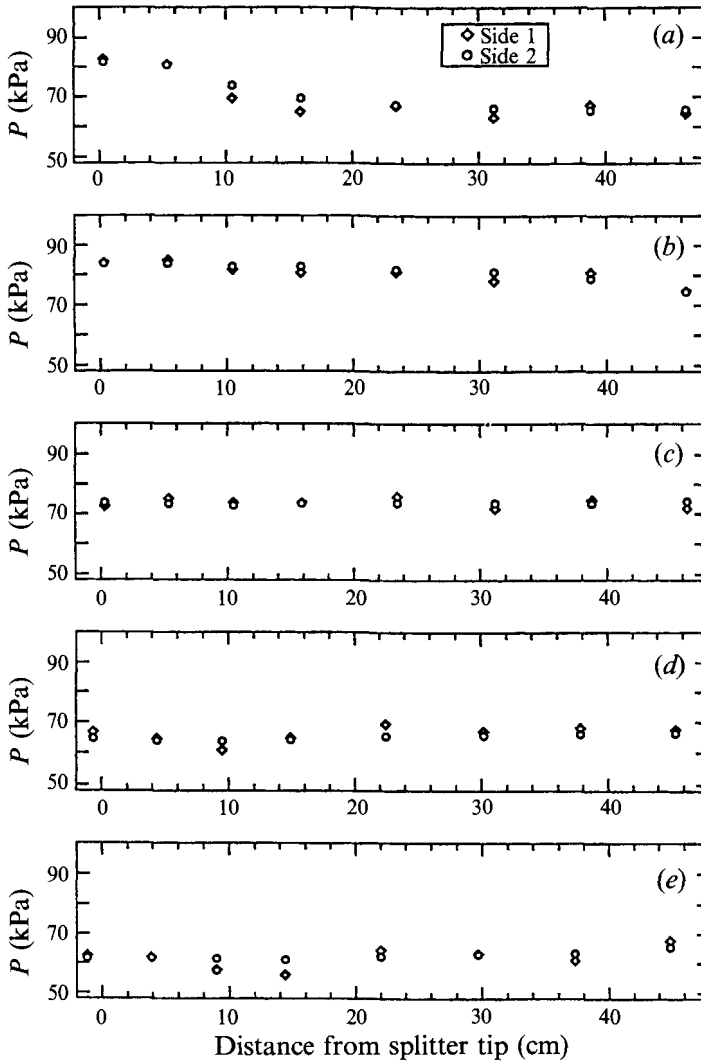


FIGURE 4. Test section static pressure distributions: (a)  $M_c = 0.28$ , (b)  $M_c = 0.42$ , (c)  $M_c = 0.50$ , (d)  $M_c = 0.62$ , (e)  $M_c = 0.79$ .

using a linear least squares fit to the last three points for the  $M_c = 0.28$  case, and the last four points for the higher Mach number cases. Only the last three points were used for the  $M_c = 0.28$  case in order to omit points taken in the accelerating flow region. In addition to Pitot thickness growth rates, for all of the cases normalized visual thickness,  $\delta_{vis}$ , growth rates are also shown. The visual thickness growth rates were obtained by fitting lines 'by eye' to the edges of time-averaged schlieren and PLMS images. The growth rate data are shown in table 3.

The growth rates were normalized by the incompressible growth rates at the same velocity and density ratios using the incompressible growth rate formula of Papamoschou & Roshko (1988):

$$\frac{d\delta}{dx} = C_\delta \frac{(1-r)(1+s^{1/2})}{1+rs^{1/2}}, \quad (4)$$

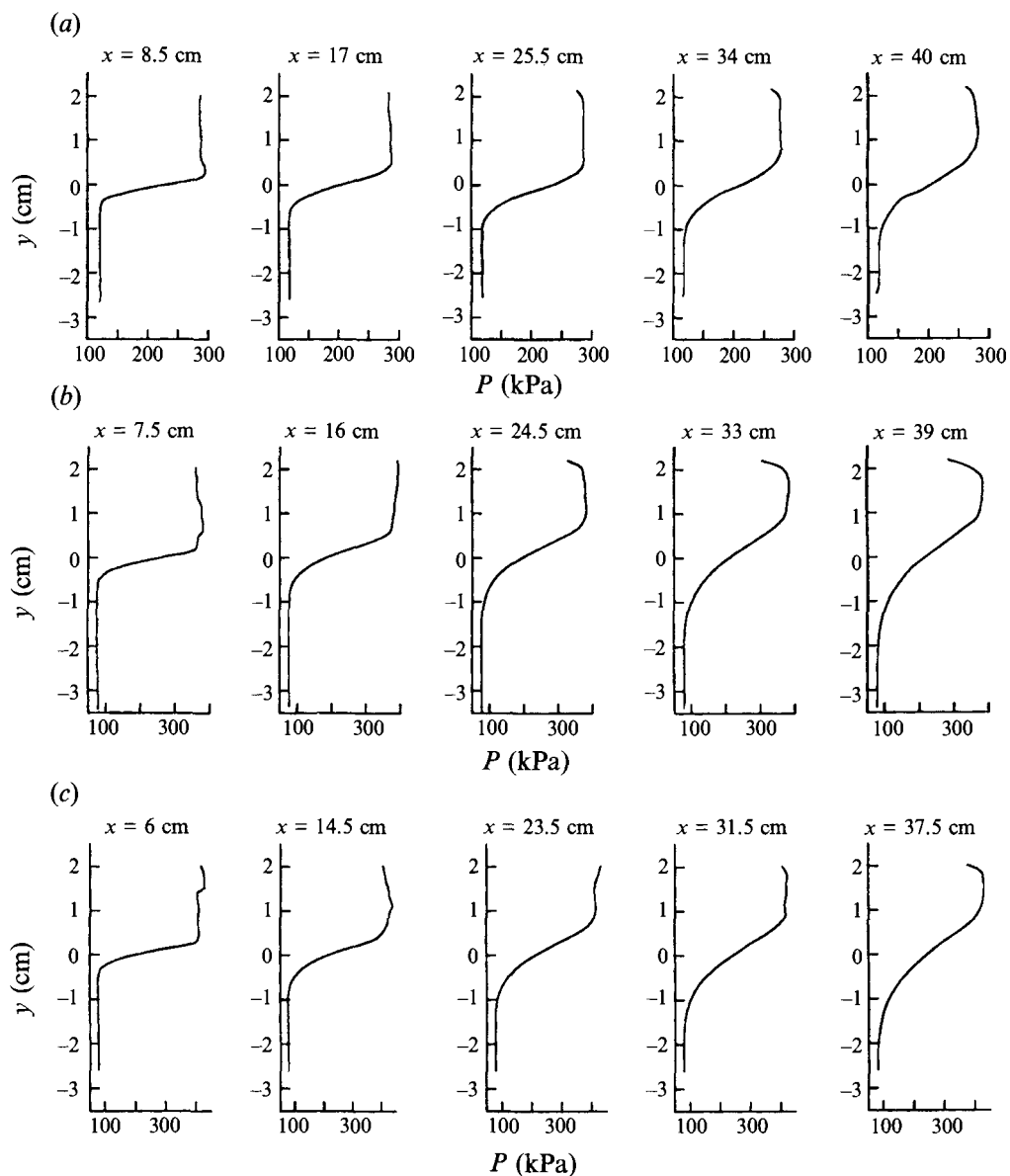


FIGURE 5. Transverse Pitot pressure profiles for several streamwise locations. Each profile is located approximately to scale with its  $x$ -location: (a)  $M_c = 0.28$ , (b)  $M_c = 0.62$ , (c)  $M_c = 0.79$ .

where  $r$  is the velocity ratio  $U_2/U_1$ ,  $s$  is the density ratio  $\rho_2/\rho_1$ , and  $C_\delta$  is a constant that depends on the particular definition of layer thickness ( $C_\delta = 0.14$  for the Pitot thickness and  $C_\delta = 0.17$  for the visual thickness). The normalized growth rates are shown in figure 7, in addition to data from other studies. The uncertainties in the present measurements are due mainly to the small sample of points used in the fit, the high-speed-side Pitot pressure non-uniformity of about 10%, and run-to-run total pressure variations of about  $\pm 2\%$ . Visual growth rates obtained using the schlieren and PLMS images gave similar results, although the procedure in general is somewhat subjective, and this is reflected in the relatively large error bars shown in the figure. Figure 7 shows

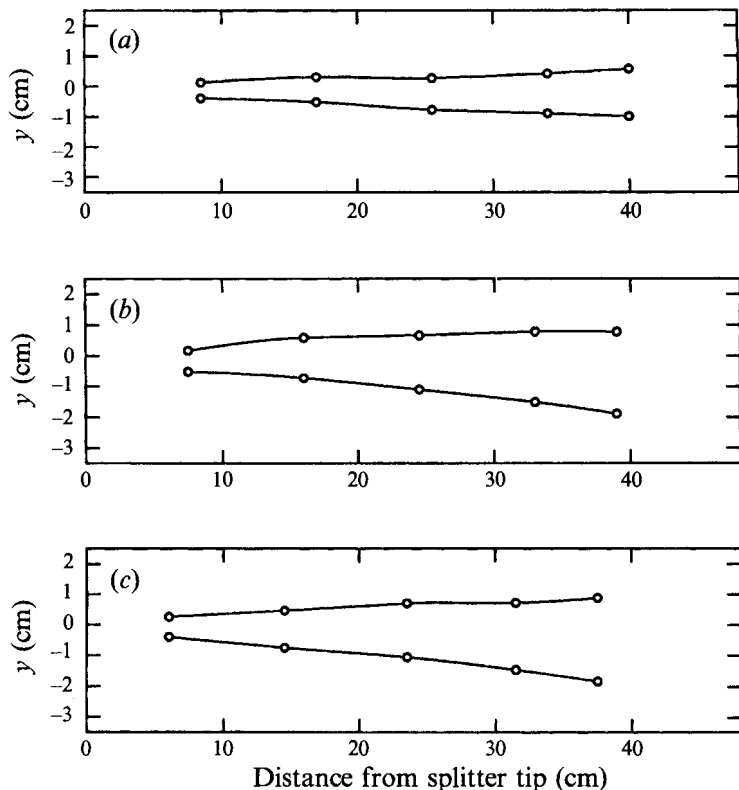


FIGURE 6.  $0.05 \Delta P_{pit}$  and  $0.95 \Delta P_{pit}$  points versus streamwise location: (a)  $M_c = 0.28$ , (b)  $M_c = 0.62$ , (c)  $M_c = 0.79$ .

Case	$M_c = 0.28$	$M_c = 0.42$	$M_c = 0.50$	$M_c = 0.62$	$M_c = 0.79$
$\delta_{pit}^* = d\delta_{pit}/dx$	0.036	—	—	0.061	0.063
$(x_0)_{pit}$ (cm)	-3.0	—	—	-4.0	-4.3
$\delta_{pit}^*/(\delta_{pit}^*)_{inc}$	0.59	—	—	0.41	0.36
$\delta_{vis}^*$	0.055	0.090	0.10	0.073	0.09
$(x_0)_{vis}$ (cm)	-4.1	-1.0	-4.0	-5.3	-6.5
$\delta_{vis}^*/(\delta_{vis}^*)_{inc}$	0.72	0.63	0.56	0.39	0.42

TABLE 3. Mixing layer growth rate data

that the present data are in general agreement with the trend of reduced normalized growth rate with increasing convective Mach number.

It should be noted in figure 7 that although the data for all of the studies shown exhibit a large amount of scatter, the results for a given study show considerably less scatter, suggesting that most of the scatter may result from systematic errors in the various experiments. For example, at the incompressible limit ( $M_c \approx 0$ ), the growth rates range from 60% to 125% of the incompressible rates. The reason for this discrepancy may be related to initial condition effects (e.g. laminar *vs.* turbulent splitter plate boundary layers), which are important if the flows had not achieved their fully developed state (Browand & Latigo 1979). In addition, the large acoustic fluctuations which are present in supersonic wind tunnels can increase the ‘flapping’ of the layer,

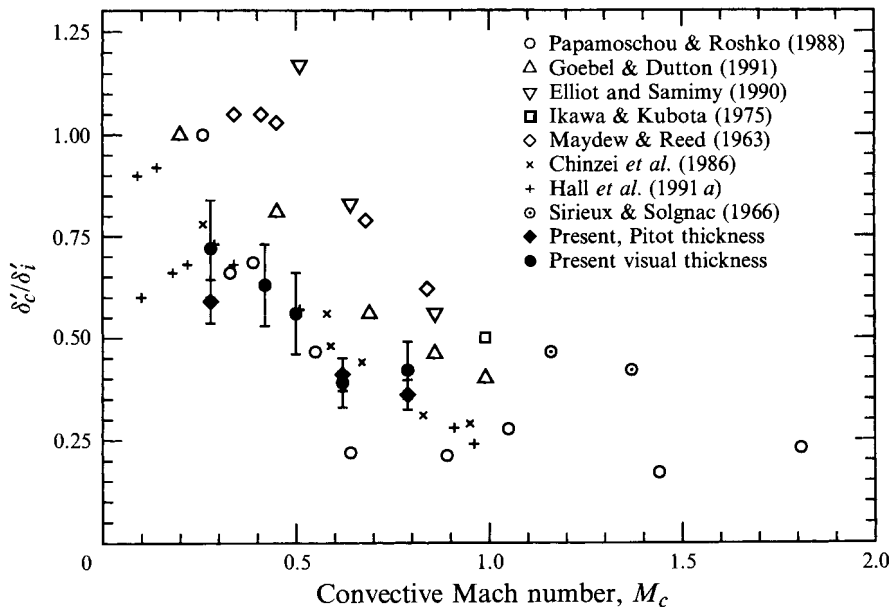


FIGURE 7. Comparison of normalized growth rate data as a function of convective Mach number.

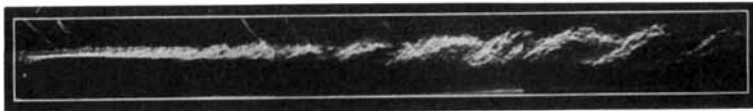


FIGURE 8. Instantaneous composite schlieren image,  $M_c = 0.28$  and  $x = 0\text{--}45$  cm. The panel is composed of three uncorrelated images 15 cm in length.

leading to higher mean growth rates. Also, as suggested by Papamoschou & Roshko (1988), compressibility may act differently on different measures of the mixing layer thickness.

#### 4.2. Schlieren and PLMS

##### 4.2.1. $M_c = 0.28$

A side view schlieren image of the entire test section, where  $x = 0\text{--}45$  cm, is shown in figure 8. The figure is a composite of three independent images of 15 cm in length. The knife edge position is horizontal and it is pushed far enough into the focused beam to block the light intensity maximum, thus rendering the background as dark, with the gradients appearing as light. Evident in figure 8 is a relatively weak shock wave from the splitter tip, and a Mach wave which originates from the supersonic nozzle/test section wall junction. The schlieren images show that coherent large-scale structures, or Brown–Roshko structures (Brown & Roshko 1974), persist to several thousand  $x/\theta_1$  downstream and to very high local Reynolds numbers ( $Re_{\delta_{vis}} \approx 380000$ ). These results are in agreement with the low convective Mach number schlieren photographs of Chinzei *et al.* (1986), but not with those of Goebel & Dutton (1991) and Hall *et al.* (1991 *a*) where Brown–Roshko structures were found to be less dominant. The differing results may be due to the schlieren visualization technique which emphasizes different types of structures depending on the position of the knife edge.

The PLMS results will be presented in the order of side ( $x, y$ ), plane ( $x, z$ ) and end

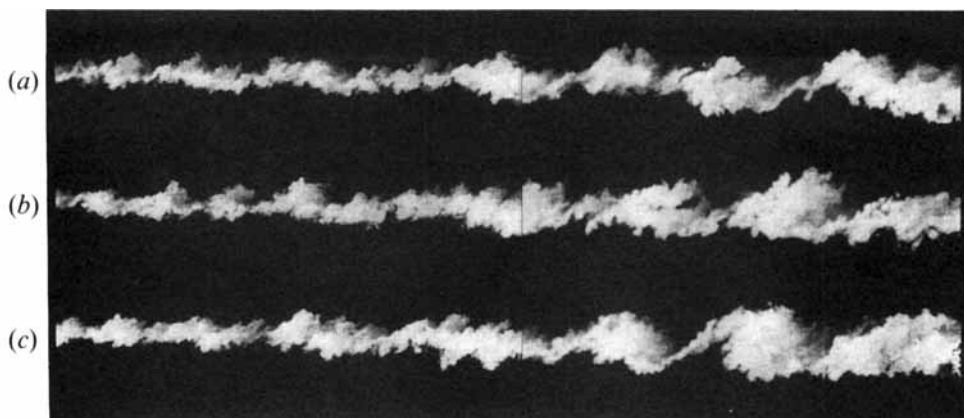


FIGURE 9. Product formation side views,  $M_c = 0.28$  and  $x = 15\text{--}45$  cm. Each panel is a composite composed of two uncorrelated images.

( $y, z$ ) views. As noted in §2, the end view was taken at an oblique angle, which results in a small amount of distortion. In all cases several realizations are shown to allow the reader to form a better impression of the layer structure.

Figure 9 shows three composite side view cuts using the product formation method where the total region imaged was  $x = 15\text{--}45$  cm. The images are composed of two 15 cm images which will be called a ‘panel’, and all of the images are uncorrelated in time. The signal-to-noise ratios (SNRs) for the product formation images are 20–25. Although all of the cuts presented here were made through the centreline of the test section ( $z = 0$  cm), no noticeable differences were seen for cuts made at  $z = 2$  cm.

The PLMS images of figure 9 reveal much more detail of the turbulent structures than the schlieren visualizations. The vortex cores, which are elliptical in shape, are composed of large amounts of mixed fluid separated by thinner braid regions which can also contain significant amounts of mixed fluid. It is of note that, in general, the structures appear more roller-like towards the downstream portion of the test section. This is also the case in the schlieren images of figure 8, and may contradict the view that the structures should degenerate into three-dimensionality with downstream distance (Chandrsuda *et al.* 1978).

Owing to the large Schmidt number of the droplets ( $Sc = 10^5\text{--}10^6$ ), it may seem unexpected that the highly strained braid regions often contain significant amounts of product (Broadwell & Breidenthal 1982). The high product levels are not surprising, however, as although the product has a large Schmidt number, the reactants (air and ethanol vapour) have Schmidt numbers of order unity.

Figure 9 also reveals details such as pairing events (last structure of *a*), and what may be a tertiary instability appearing as a sequence of bumps on the braid structures and vortex cores (second to last structure of *c*). Figure 9 also shows that the cores are not completely uniform, but can exhibit a large variation in signal.

Figure 10 shows composite side views using the passive scalar method where  $x = 15\text{--}45$  cm and  $z = 0$  cm. The SNR for the passive scalar images was about 15–18, somewhat lower than for the product formation images. The figure shows that the passive scalar method also reveals the domination of the layer by coherent structures. This is particularly evidenced by the large intrusions of free-stream fluid into the layer. The low-speed fluid intrusions, which are black, appear to be deeper than is actually the case (see, for example, *b*), owing to the limited dynamic range of the reproduction, and also to the possible evaporation of the droplets. This is seen by comparing to

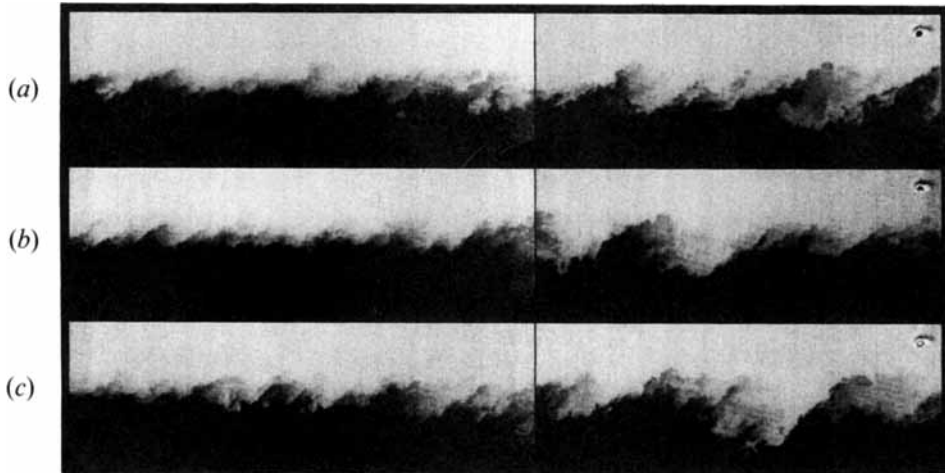


FIGURE 10. Passive scalar side views,  $M_c = 0.28$  and  $x = 15\text{--}43$  cm. Each panel is a composite composed of two uncorrelated images.

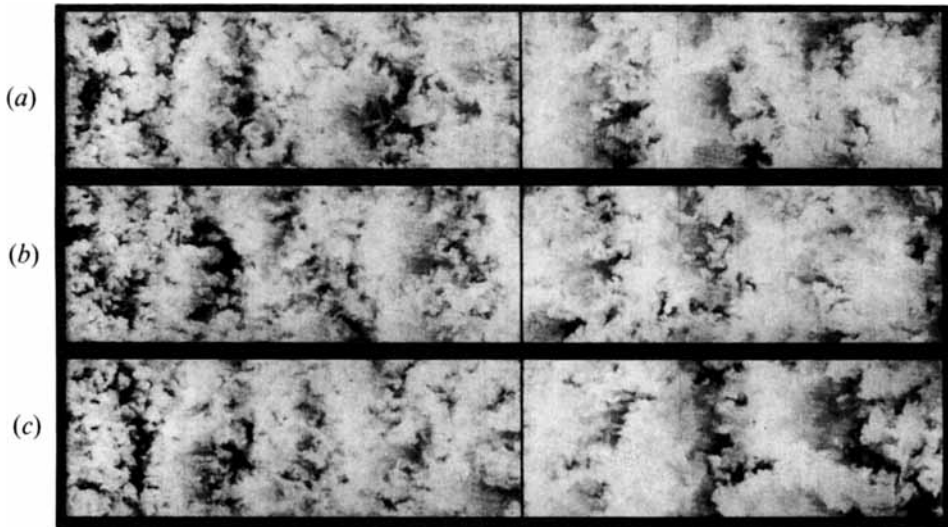


FIGURE 11. Product formation plan views through the middle of the layer,  $M_c = 0.28$ ,  $x = 15\text{--}45$  cm,  $z = -2.5\text{--}2.5$  cm and  $y = 0$  cm. Each panel is a composite composed of two uncorrelated images.

figure 9 where regions of pure low-speed fluid are rarely seen to cross the centreline of the layer. The bumps from the above-mentioned tertiary instability are also seen in figure 10 in the last structure of (a).

Owing to the contrast in the scattering signals, the product formation method emphasizes turbulent motions which bring mixed fluid next to unmixed fluid, whereas the passive scalar method emphasizes motions which bring pure high-speed fluid next to pure low-speed fluid. Therefore, the product formation method emphasizes the structure cores, while the passive scalar method emphasizes the braids, which are thin regions bordering high- and low-speed fluid.

Plan view product formation images are shown in figure 11, where  $x = 15\text{--}45$  cm,  $z = -2.5\text{--}2.5$  cm, and the laser sheet is at the splitter tip level ( $y = 0$  cm) which roughly corresponds to the middle of the mixing layer. The test section sidewalls are at  $z = -5$

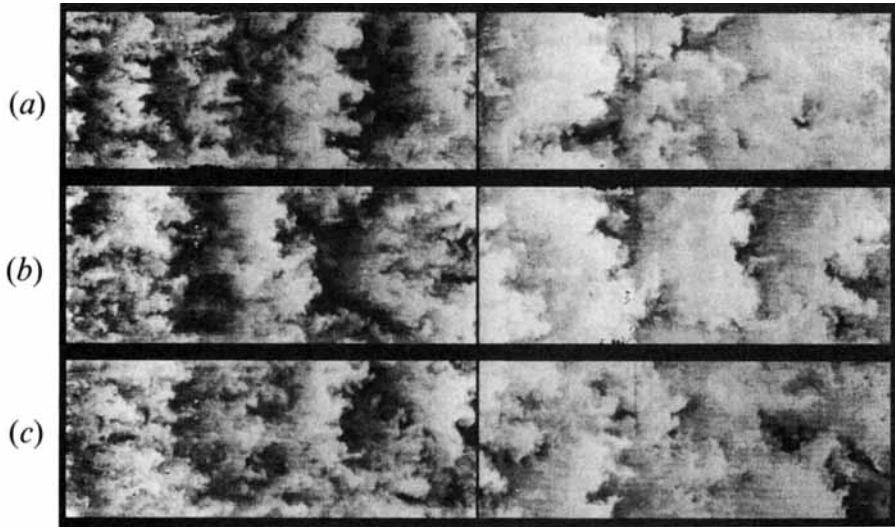


FIGURE 12. Passive scalar plan views through the middle of the layer,  $M_c = 0.28$ ,  $x = 15\text{--}42$  cm,  $z = -2.5\text{--}2.5$  cm and  $y = 0$  cm. Each panel is composed of two uncorrelated images.

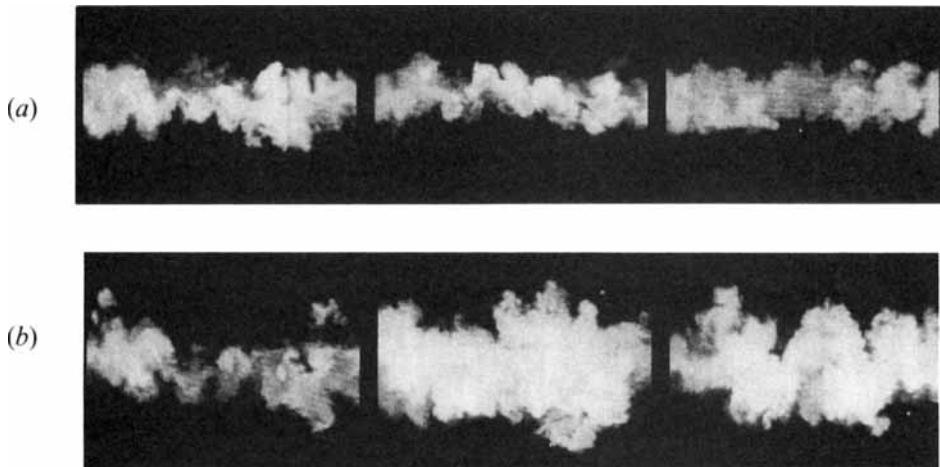


FIGURE 13. Product formation end views,  $M_c = 0.28$  and  $z = -2.5\text{--}2.5$  cm  
(a)  $x = 19$  cm, (b)  $x = 34$  cm.

and 5 cm, thus the boundary layers are not in the field of view. In many of these images the structures span the width of the field of view in agreement with previous studies in incompressible flow (Brown & Roshko 1974; Wygnanski *et al.* 1979; Browand & Troutt 1985; Bernal & Roshko 1986). Unlike the lower Reynolds number results of Brown & Roshko and Bernal & Roshko, however, the structures often appear skewed and bent, in agreement with the results of Browand & Troutt (1985). Furthermore, the structures are connected by smaller oblique structures which may be related to the helical pairings found by Chandrsuda *et al.* (1978). As with the side views, the mixing layer sometimes appears highly irregular with no apparent organization.

Passive scalar plan view images through the middle of the layer are shown in figure 12, where the sheet and camera locations are the same as in figure 11. In agreement with the product formation images, the passive scalar images also reveal the quasi-two-

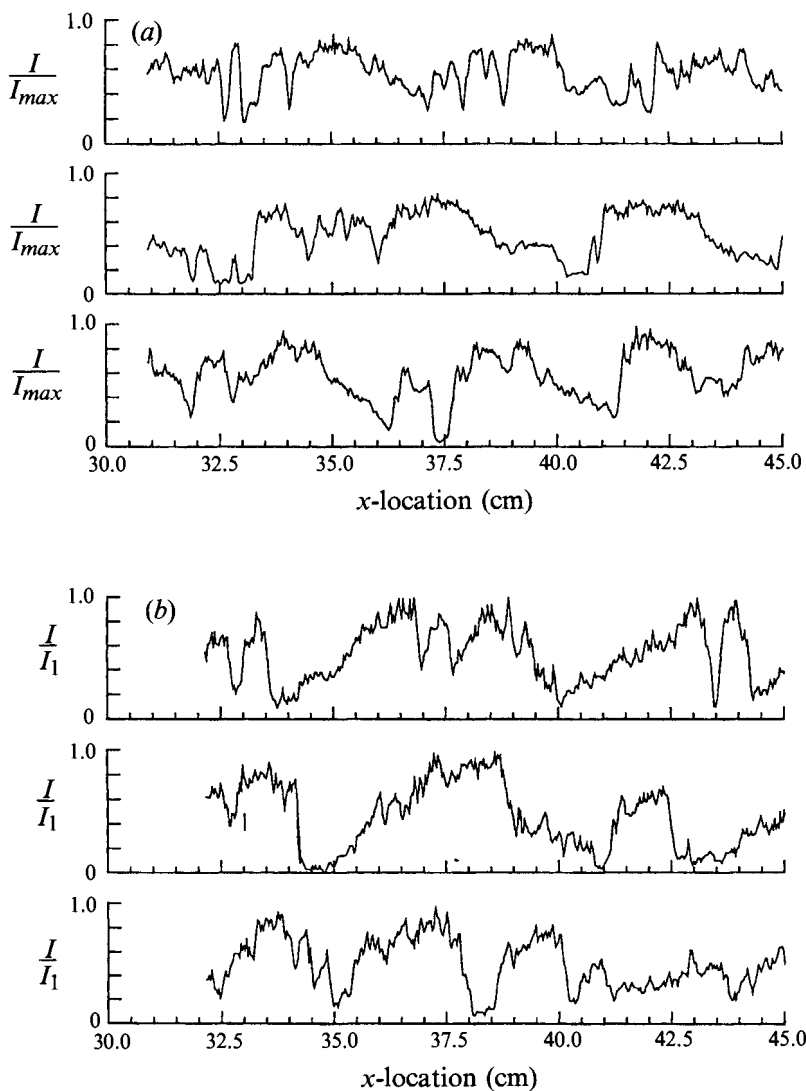


FIGURE 14. Streamwise signal intensity profiles through  $M_c = 0.28$  side view images for (a) the production formation method and (b) the passive scalar method.

dimensionality of the structures. The structures seen in figures 11 and 12 are not the same, however, since with the product formation method, the cores appear as white bands, whereas with the passive scalar method the white bands result from intrusions of pure high-speed fluid between the structures. The vortex cores, in figure 12, appear as the grey regions to the left of these white bands. Also very apparent in figure 12, are the streamwise braid vortices (bright-dark intersections) observed in low-speed incompressible mixing layers (Bernal & Roshko 1986). These vortices are seen to be quite prominent at this very large Reynolds number.

Typical end view cuts using the product formation method are shown in figure 13 for  $x = 19$  and  $34$  cm and  $z = -2.5$ – $2.5$  cm. The trends are best seen in the  $x = 34$  cm cuts where the images often appear as thick regions of mixed fluid which may correspond to cuts through the cores of the Brown–Roshko structures. Sometimes thinner highly

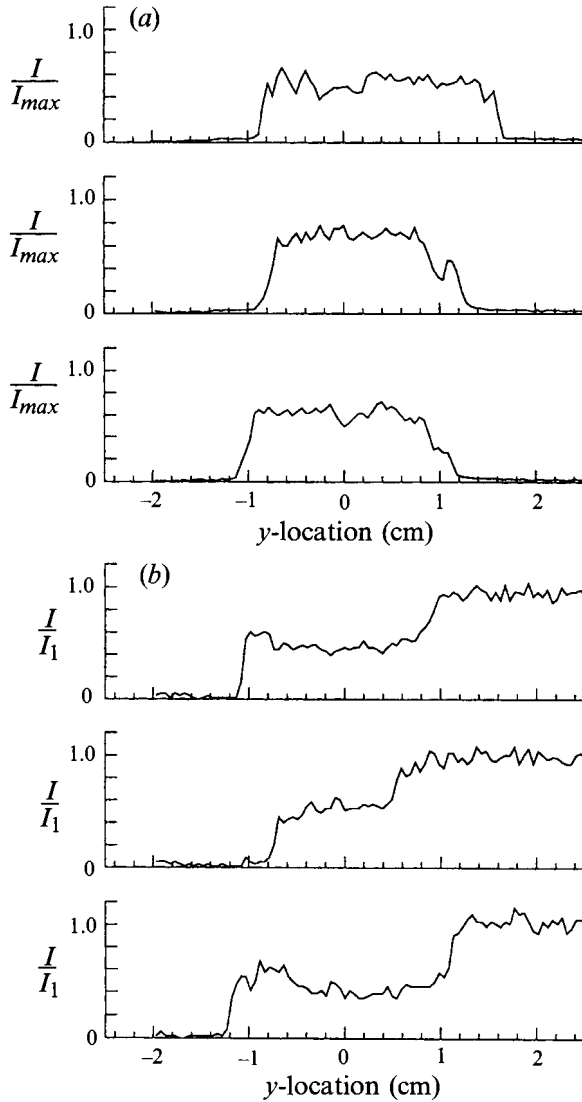


FIGURE 15. Cross-stream signal intensity profiles through  $M_c = 0.28$  side view images for (a) the product formation method and (b) the passive scalar method.

convoluted structures are observed and probably correspond to cuts through the braid regions between the structures. It is also of note that the signal intensity is seen to be relatively uniform across the cores whereas it is highly variable across the braids. End view passive scalar images were made for some of the cases but owing to poor quality are not shown.

Information concerning the state of mixing in the layer can be obtained by considering the actual signal levels of the fog images. This is shown in figure 14 where three intensity profiles through the product formation and passive scalar side views are compared. The product formation profiles were normalized by the maximum signal of the three profiles, while the passive scalar profiles were normalized by the high-speed free-stream intensity. These profiles were taken at the  $y$ -location corresponding to the peak in the mean product formation profile. Figure 14 shows that the signals often

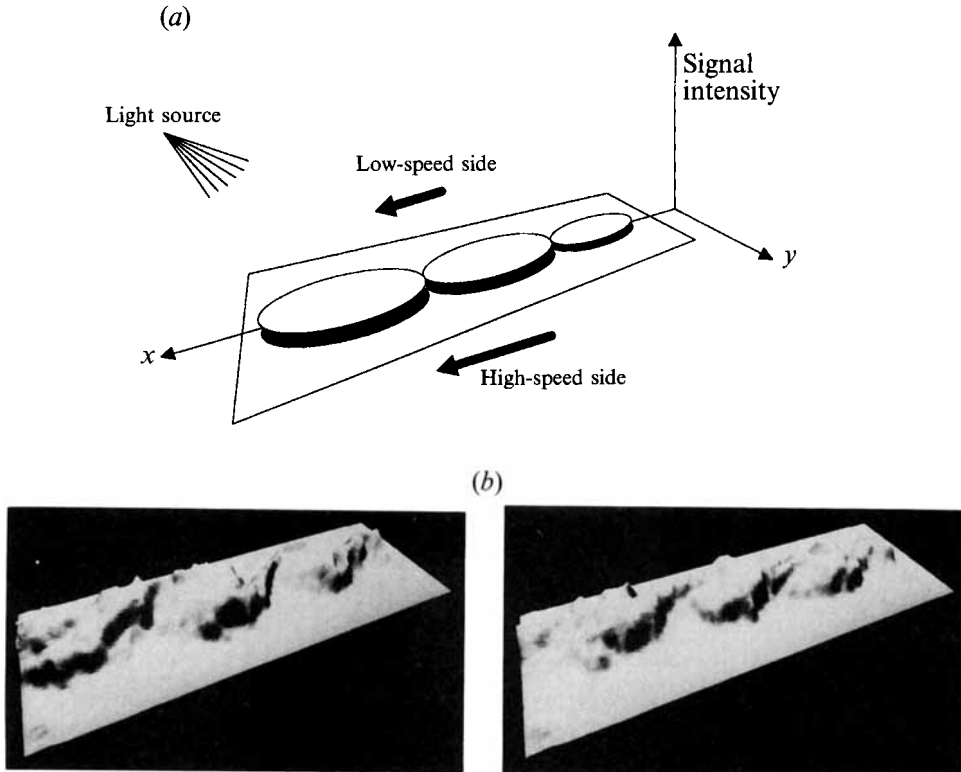


FIGURE 16. (a) Schematic diagram showing the axes orientation and light source location for the perspective views. (b) Perspective views of  $M_c = 0.28$  product formation side view images,  $x = 15-30$  cm.

exhibit negatively and positively sloped regions for the product formation and passive scalar methods, respectively. These sloped regions are similar to the 'sawtooth' or sloped temperature traces observed by Fiedler (1974) in an incompressible planar mixing layer where one stream was slightly heated. Fiedler argued that the sloped traces are due to the vortex core concentration being biased to the side from which it entrains free-stream fluid. This causes the sign of the slope to depend on whether the high- or low-speed free stream was heated. The product formation profiles also show remarkable resemblance to the incompressible reacting mixing layer product time traces of Mungal & Dimotakis (1984) where the signals are sloped and reveal that pure fluid only rarely reaches the middle of the layer.

Cross-stream ( $y$ -direction) profiles through select structures are shown in figure 15. The figure shows that the cross-stream scattering profiles for the product formation method can be 'top hat' shaped, suggesting that the structures are relatively uniform in this direction, in agreement with Fielder. The passive scalar profiles also show this uniformity as seen by the stepped profiles of figure 15.

Additional details of the mixing can be seen by considering the four product formation side views shown in perspective in figure 16, where  $x = 30-45$  cm. The perspective views were generated by mapping the signal intensities into elevation and rendering it as a volume consisting of a solid surface. A point source of light is then used to illuminate the surface. Elevation, therefore, represents the signal intensity while the light and dark regions are shadows which aid the eye in determining the elevation.

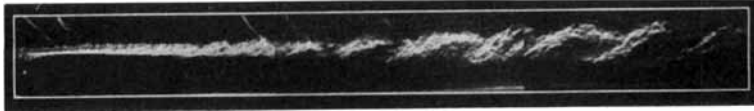


FIGURE 17. Composite schlieren image,  $M_c = 0.42$  and  $x = 0-45$  cm.

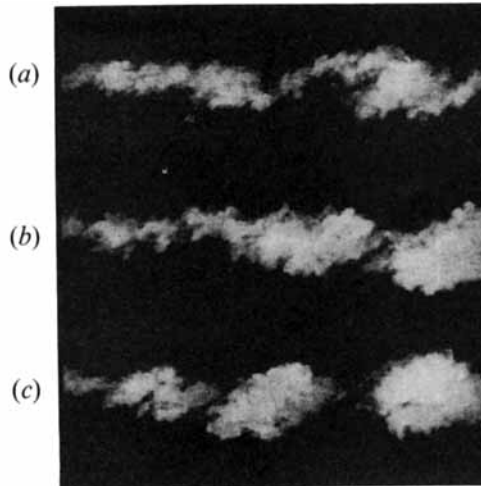


FIGURE 18. Side view product formation images,  $M_c = 0.42$  and  $x = 15-30$  cm.

As shown in figure 16(a), the point of view is from the high-speed side looking toward the low-speed side; thus the flow is from right to left with the low-speed side on top. The images in figure 16(b) show that the layer consists of relatively distinct vortex cores separated by the braid regions which often exhibit large gradients. In agreement with the profiles, the core concentrations are sloped in the streamwise direction but more uniform in the cross-stream direction.

#### 4.2.2. $M_c = 0.42$

A composite schlieren image for the  $M_c = 0.42$  case, extending from  $x = 0$  to 45 cm, is shown in figure 17. As with the lower convective Mach number case, Brown-Roshko structures dominate the layer. For this case the local Reynolds number,  $Re_{\delta_{vis}} > 700000$  at the exit of the test section.

Side view product formation images are shown in figure 18 where the imaged region is  $x = 15-30$  cm. The structures seen in figure 18 are similar to those for the  $M_c = 0.28$  case, but are also subtly different. The main difference is that the structures appear less elliptical and typically have a more disorganized appearance. This is not believed to be a Reynolds number effect because the difference is apparent even at streamwise locations where the Reynolds numbers are equal (e.g. at  $x = 45$  cm for  $M_c = 0.28$  and at  $x = 15$  cm for  $M_c = 0.42$ ). Plan views through the middle of the layer ( $y = 0$  cm) are shown in figure 19 and show that the structures remain quasi-two-dimensional. Nevertheless, they appear even more skewed than found for  $M_c = 0.28$ . The end views of figure 20, located at  $x = 18.5$  cm and  $z = -2.5-2.5$  cm, appear qualitatively similar to the  $M_c = 0.28$  case where either thick cores or thin convoluted braids are observed. Again, the cores tend to exhibit a relatively uniform concentration.

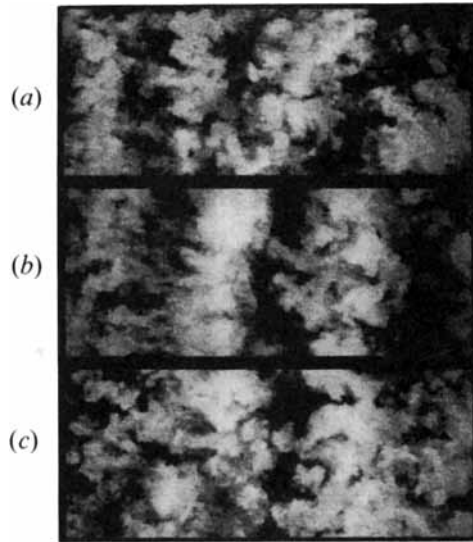


FIGURE 19. Plan view product formation images,  $M_c = 0.42$ ,  $x = 15\text{--}30$  cm and  $y = 0$  cm.

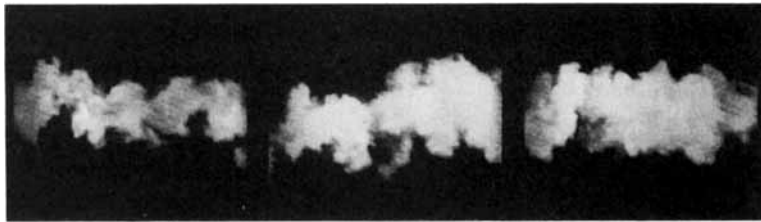


FIGURE 20. End view product formation images,  $M_c = 0.42$ ,  $x = 18.5$  cm and  $z = -2.5\text{--}2.5$  cm.

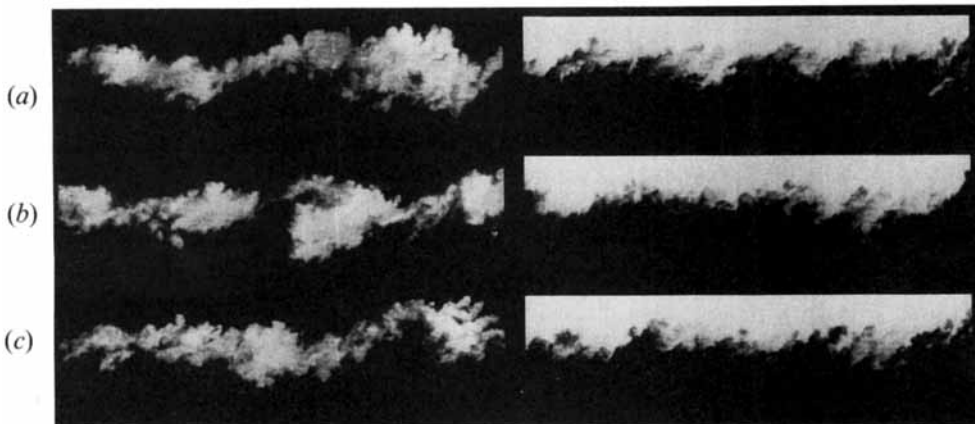


FIGURE 21. Side view images,  $M_c = 0.50$  and  $x = 15\text{--}30$  cm. Product formation and passive scalar images are at the left and right, respectively.

#### 4.2.3. $M_c = 0.50$

Product formation and passive scalar fog images at  $M_c = 0.50$  are shown in figure 21. Only fog side views were obtained for this case, thus schlieren images and fog plan and end views are not shown. The imaged region is  $x = 15\text{--}30$  cm and  $Re_{\delta vis} = 700\,000$

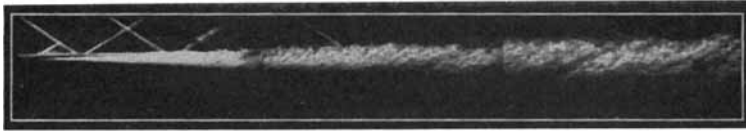


FIGURE 22. Composite schlieren image,  $M_c = 0.62$  and  $x = 0\text{--}45$  cm.

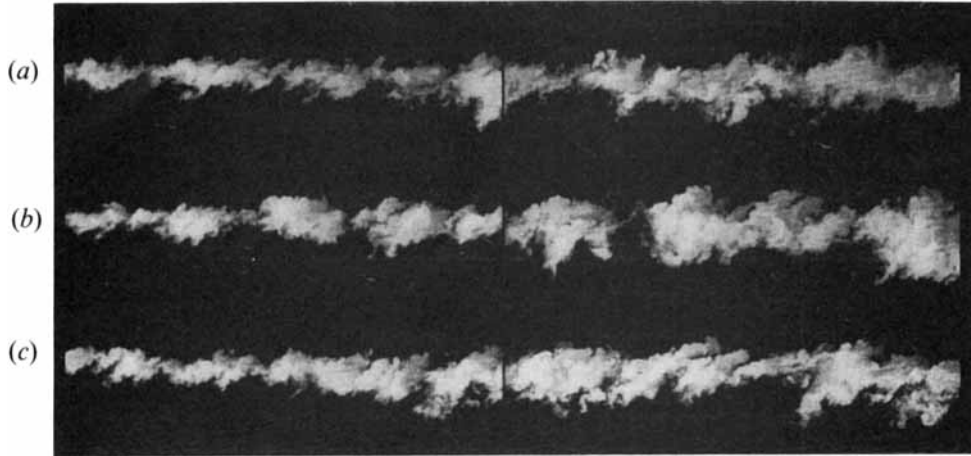


FIGURE 23. Product formation side views,  $M_c = 0.62$  and  $x = 15\text{--}45$  cm.

at  $x = 30$  cm. This figure shows that rollers are also apparent at this convective Mach number, although we can generalize that the layer appears to be less organized than the lower convective Mach number cases. Although large-scale rollers are often present, as with the  $M_c = 0.42$  case, they are not elliptical, but instead appear more irregular and are almost polygonal (e.g. *b*). This change in shape will be discussed further in §4.3.

#### 4.2.4. $M_c = 0.62$

A composite schlieren image covering the entire test section for the  $M_c = 0.62$  case is shown in figure 22. At this higher convective Mach number, the Brown–Roshko rollers are not readily identifiable, although large-scale structures are observed near the end of the test section. The structures appear as irregularly spaced bands that are oriented at a dominant angle of about  $30^\circ$  from the horizontal. Similar indistinct structures can be found in the schlieren photographs of Papamoschou & Roshko (1988) and Goebel & Dutton (1991).

Figure 23 shows product formation side view cuts where  $x = 15\text{--}45$  cm,  $z = 0$  cm and  $Re_{\delta_{vis}} = 10^6$  and  $x = 45$  cm. This figure shows that the layer is composed of large-scale structures, but they rarely appear as the coherent Brown–Roshko type. Although Brown–Roshko structures are rare, possible examples are seen in (*b*) (left). As shown by Clemens & Mungal (1992*a*), the structures of figure 23 appear more irregular, with the high- and low-speed side interfaces often appearing more jagged than at  $M_c = 0.28$ . The jagged interfaces may be due to an increase in the number of small-scale structures which cause sharp intrusions into the layer. Passive scalar side view images are shown in figure 24 and similarly show these irregular structures. Taken as a whole, figures 23 and 24 show that there is considerable variation in structure among the different realizations.

Figure 25 shows product formation plan view cuts through approximately the

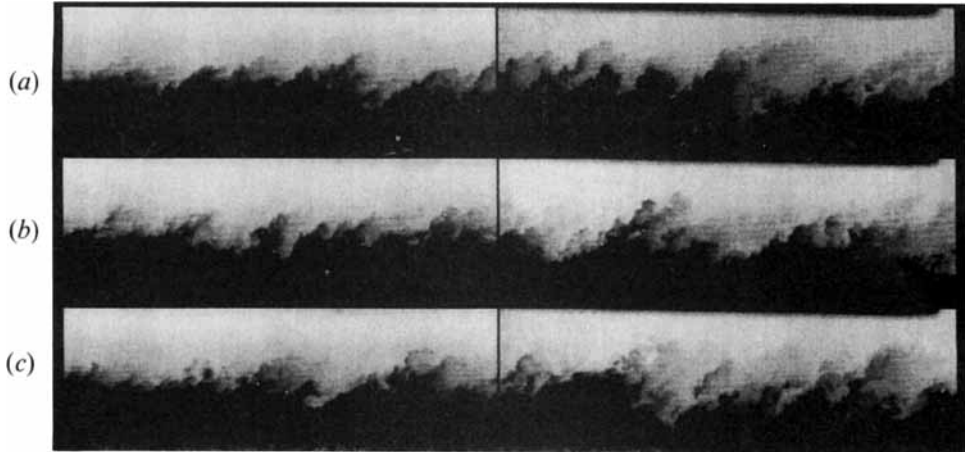


FIGURE 24. Passive scalar side views,  $M_c = 0.62$  and  $x = 15\text{--}45$  cm.

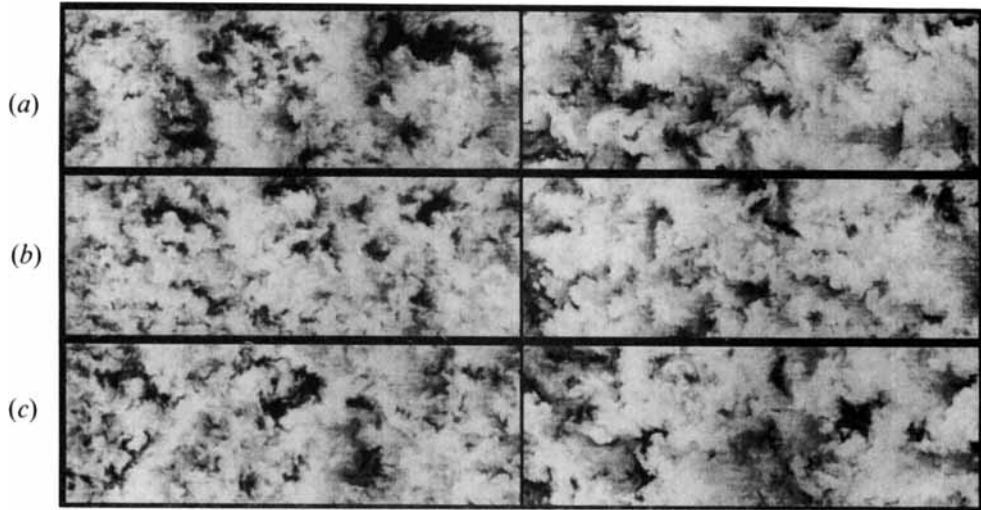


FIGURE 25. Product formation plan views through the middle of the layer,  $M_c = 0.62$ ,  $x = 15\text{--}45$  cm,  $z = -2.5\text{--}2.5$  cm and  $y = 0$  cm.

middle of the layer ( $y = 0$  cm) where  $x = 15\text{--}45$  cm and  $z = -2.5\text{--}2.5$  cm. These plan view images show that the structures are not nearly as two-dimensional as at the lower convective Mach number. Sometimes skewed spanwise bands occur although they are not usually followed, nor preceded, by other spanwise bands (*a*, left). This is consistent with the side views where only occasional rollers are seen. In some of the images (*a*, left) oblique structures can be seen, but they do not appear to be a dominant feature of the flow. In general, these plan view cuts appear highly three-dimensional and apparently lack any obvious spatial regularity or organization.

Passive scalar plan views are shown in figure 26 where the imaged region and sheet location are the same as in figure 25. These images are consistent with the highly three-dimensional character seen with the product formation method. Since these passive scalar images will emphasize turbulent motions which bring pure non-seeded low-speed fluid into the layer, it is seen from randomly oriented dark patches that these motions are neither primarily spanwise nor streamwise.

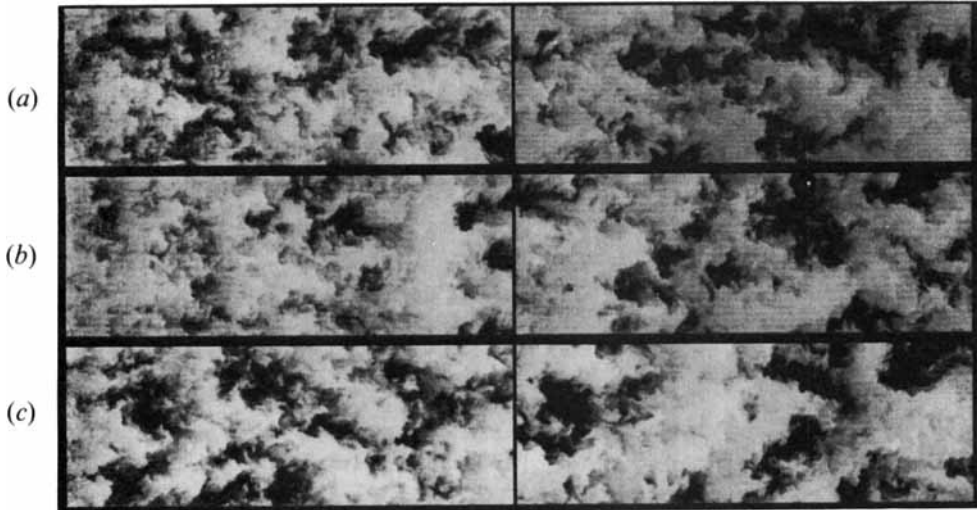


FIGURE 26. Passive scalar plan views through the middle of the layer,  $M_c = 0.62$ ,  $x = 15\text{--}45$  cm,  $z = -2.5\text{--}2.5$  cm and  $y = 0$  cm.

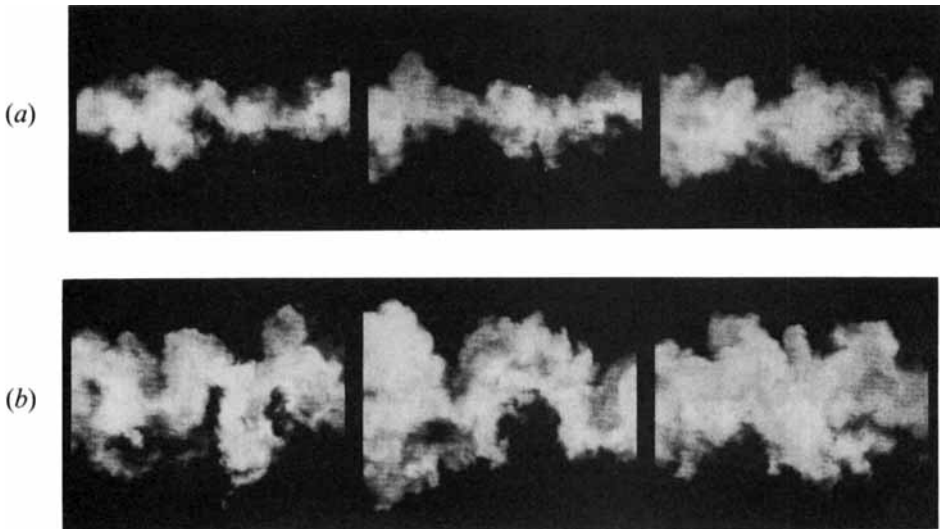


FIGURE 27. Product formation end views,  $M_c = 0.62$  and  $z = -2.5\text{--}2.5$  cm: (a)  $x = 22$  cm, (b)  $x = 36.5$  cm.

Figure 27 shows product formation end view cuts at the  $x = 22$  and  $36.5$  cm locations, where the imaged region is  $z = -2.5\text{--}2.5$  cm. While these images appear similar to the  $M_c = 0.28$  case, there are some differences. The first difference is that the images cannot be easily characterized as cuts through the vortex core or braid regions as was possible at  $M_c = 0.28$  and  $0.42$ . In contrast to the lowest convective Mach numbers most of the end views are highly convoluted suggesting that the layer is more dominated by streamwise vorticity. Also seen are what appear to be mushroom structures caused by counter-rotating vortices (left image of figure 27*b*). Another difference from the lower compressibility cases is that the structure signal levels are less uniform.

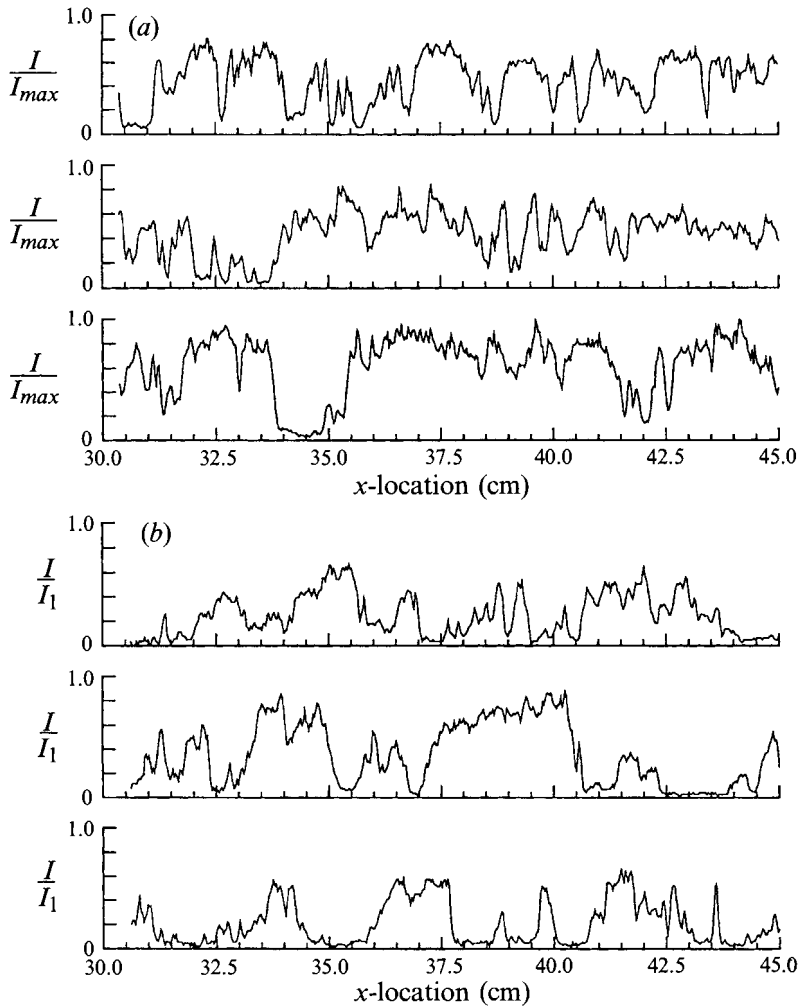


FIGURE 28. Streamwise signal intensity profiles through  $M_c = 0.62$  side view images for (a) the product formation method and (b) the passive scalar method.

In order to see how these structural differences are reflected in the mixing, signal intensity profiles are shown in figure 28. These profiles show that although streamwise sloped signals are found, they are not as dominant as at  $M_c = 0.28$ . This provides evidence that the entrainment of fluid does not occur through predominantly spanwise motions, in agreement with the plan view visualizations. Sloped structures do sometimes appear, however, thus some spanwise motions are undoubtedly present. Cross-stream profiles are shown in figure 29 and show that the structures can be uniform in the cross-stream direction, but can also exhibit considerable variation. This is seen especially in the passive scalar profiles, where the signals appear both stepped and linearly sloped from the lowest to the highest signal levels.

Perspective views of selected product formation images for the  $x = 30\text{--}45$  cm station are shown in figure 30. The orientation of the axes is as shown in figure 16(a), thus the flow moves from right to left with the low-speed fluid on top. The perspective views show the irregular nature of the structures, especially the jagged high- and low-speed interfaces discussed above. This figure also shows that the structures exhibit

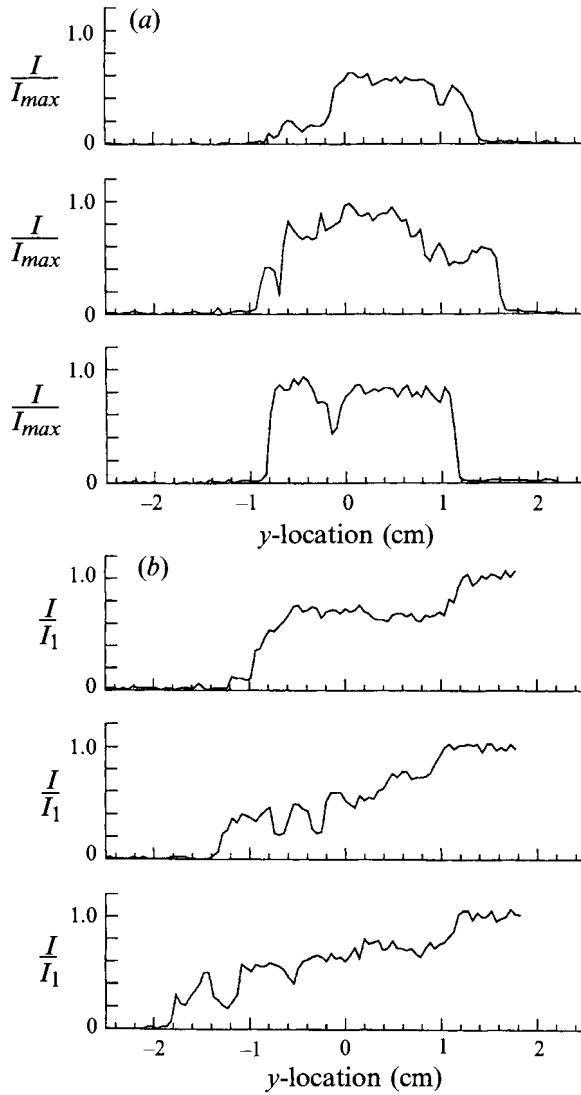


FIGURE 29. Cross-stream signal intensity profiles through  $M_c = 0.62$  side view images for (a) the product formation method and (b) the passive scalar method.

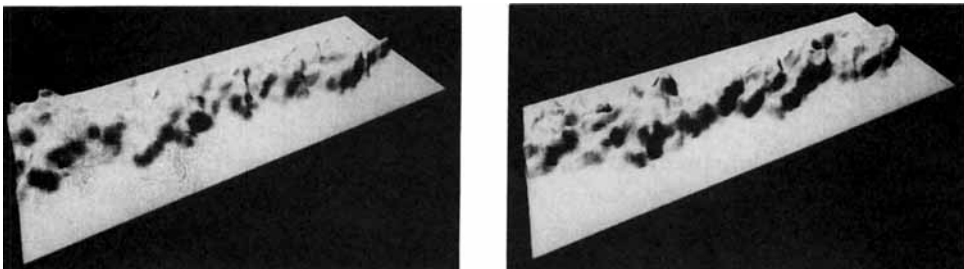


FIGURE 30. Perspective views of  $M_c = 0.62$  product formation side view images,  $x = 15\text{--}30$  cm.

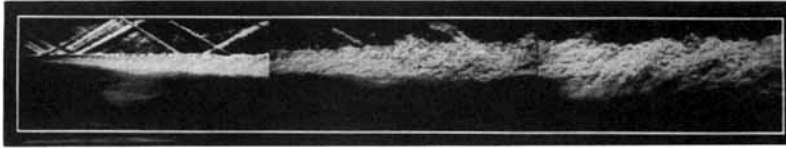


FIGURE 31. Composite schlieren image,  $M_c = 0.79$  and  $x = 0-45$  cm.

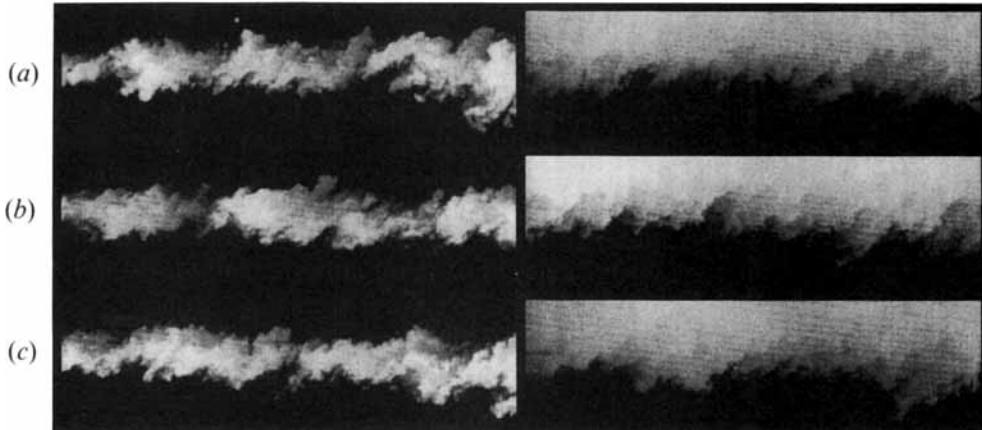


FIGURE 32. Side view images,  $M_c = 0.79$  and  $x = 18-33$  cm. Product formation and passive scalar images are at the left and right, respectively.

significantly more variation in the cross-stream direction than the  $M_c = 0.28$  case. It is interesting that many of the structures appear to be aligned with a dominant angle in agreement with McIntyre & Settles (1991) and the schlieren images of figure 22.

#### 4.2.5. $M_c = 0.79$

Figure 31 shows a side view schlieren composite image of the entire test section for the  $M_c = 0.79$  case. As with the  $M_c = 0.62$  case, the only evidence for large-scale structures is the inclined bands near the end of the test section.

Side view planar visualizations are shown in figure 32, where the product formation and passive scalar images are shown on the left and right, respectively, for  $x = 18-33$  cm. This figure shows that the structure is similar to the  $M_c = 0.62$  case, where rollers are rare and both high- and low-speed interfaces appear jagged.

Plan view cuts through the middle of the layer for  $x = 18-33$  cm,  $z = -2.5-2.5$  cm and  $y = 0$  cm are shown in figure 33, where the product formation and passive scalar methods are shown on the left and right, respectively. The product formation images (left) show the highly three-dimensional structure that is characteristic of the  $M_c = 0.62$  case, with no obvious spanwise, streamwise or oblique organization. The passive scalar images (right) are also three-dimensional, but additionally show some evidence of streamwise structure.

End views using the product formation method are shown in figure 34, where  $x = 18$  and 32 cm. Again the layer is seen to be highly convoluted suggesting that streamwise (or oblique) motions are present. Similar streamwise motions were observed in the axisymmetric mixing layer measurements of Fourquette *et al.* (1990). Also of note in these end views is that some of the images appear to be composed of two distinct regions of mixed fluid. This is seen in figure 34(b), where distinct low- and high-signal regions appear on the top and bottom of the layer, respectively. These

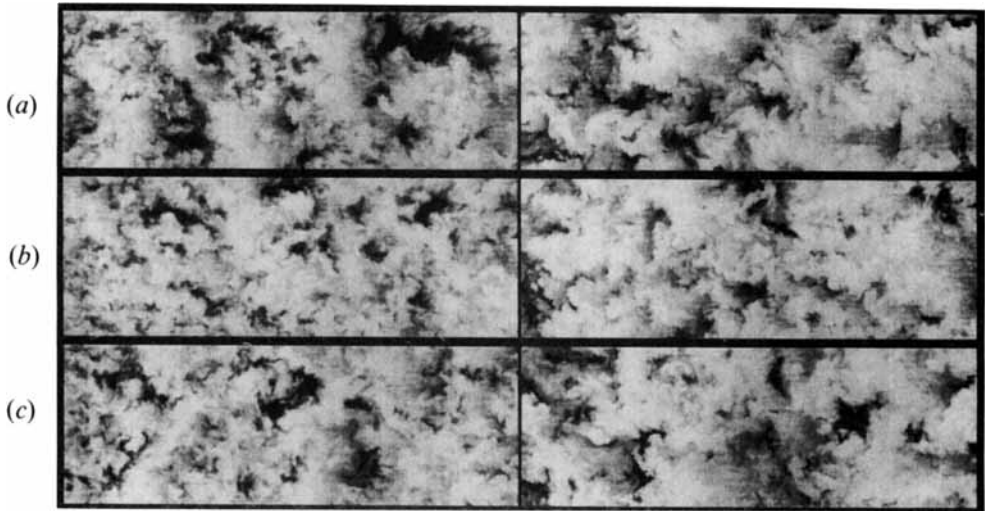


FIGURE 33. Plan view images through the middle of the layer,  $M_c = 0.79$ ,  $x = 18\text{--}33$  cm,  $z = -2.5\text{--}2.5$  cm and  $y = 0$  cm. Product formation and passive scalar images are at left and right, respectively.

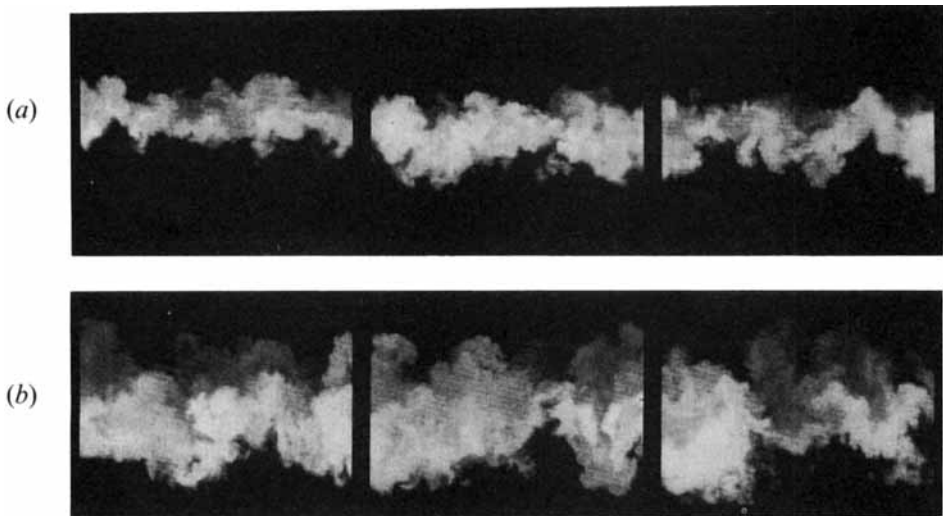


FIGURE 34. Product formation end views,  $M_c = 0.79$  and  $z = -2.5\text{--}2.5$  cm:  
(a)  $x = 18$  cm, (b)  $x = 32$  cm.

images should be contrasted with the more uniform end view structures of figure 13(b). This double-level characteristic is sometimes apparent in the side view images of figure 32, where regions of low signal are present along the high-speed side interface (b, left).

Streamwise signal intensity profiles are shown in figure 35 where the signals are sometimes sloped, but not predominantly so. Cross-stream profiles through select structures are shown in figure 36 and reveal a subtle difference from the profiles of the  $M_c = 0.28$  case. The primary difference is that the structure scattering signals are not uniform but are biased toward the side to which they are closest. This is seen in the product formation profiles as the negative slopes and less clearly in the passive scalar profiles as the positive slopes. Some of these profiles also appear to be composed of two regions of relatively uniform fluid, as seen in the third product formation profile and

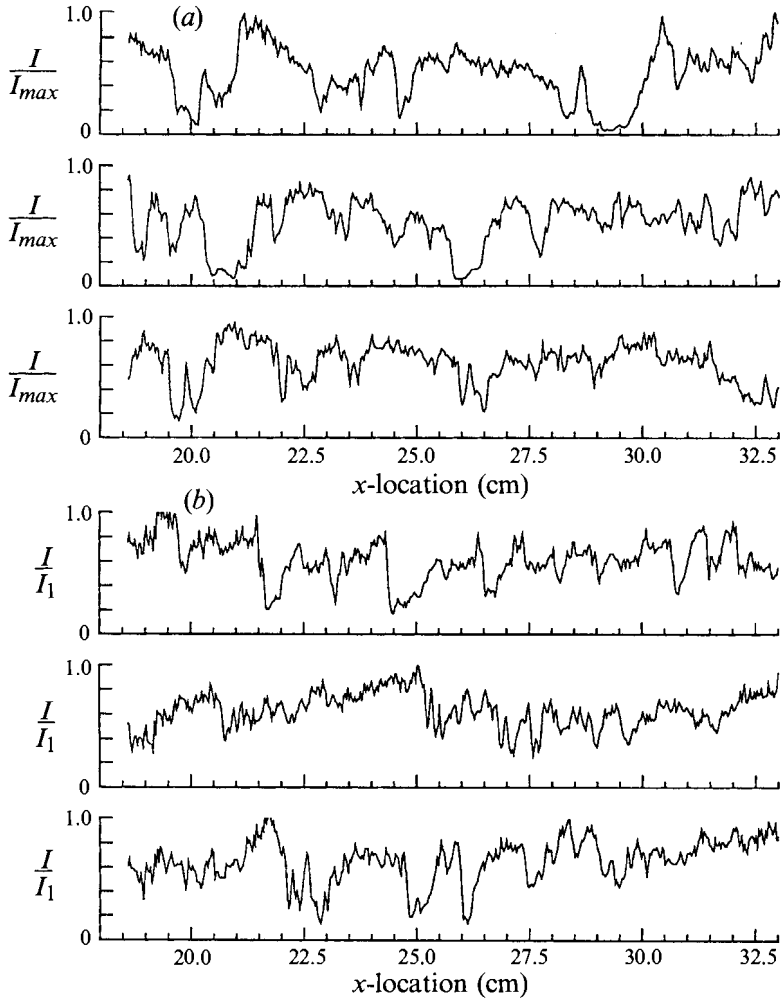


FIGURE 35. Streamwise signal intensity profiles through  $M_c = 0.79$  side view images for (a) the product formation method and (b) the passive scalar method.

the second passive scalar profile. These separate regions of mixing are easier to see in the side views of figure 32 (b, left), and in the end view of figure 34(b), where light and dark regions are observed on the low- and high-speed sides, respectively.

Some of these features are further seen in the perspective views of select product formation side views shown in figure 37, where the axes are defined as in figure 16(a). Many of the structures are irregular, with jagged high- and low-speed side interfaces.

#### 4.3. Discussion of the PLMS results

It has been shown that the mixing layer makes a clear transition from quasi-two-dimensionality at low convective Mach number, to three-dimensionality at moderate convective Mach number. Perhaps related to this transition is what appears to be a change in the nature of the spanwise rollers with increasing convective Mach number. This is shown in figure 38(a) where several (presumed) rollers are shown at convective Mach numbers of 0.28, 0.42, 0.50 and 0.62 using the PLMS product formation technique. At  $M_c = 0.28$ , the roller cores appear relatively 'round' or 'elliptical', but become progressively more 'square' or 'polygonal' at higher  $M_c$ . This change is shown

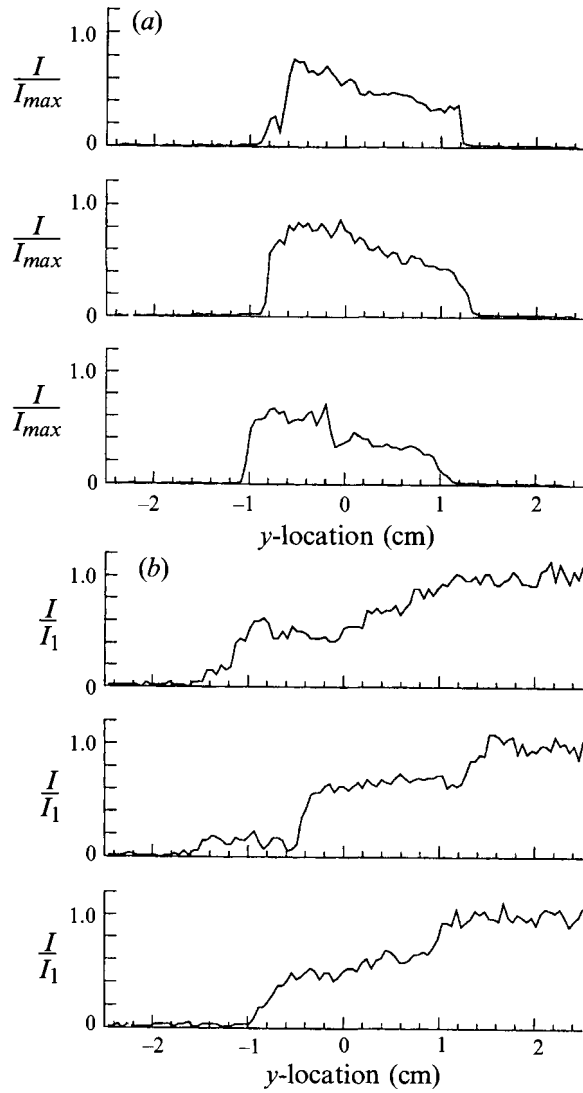


FIGURE 36. Cross-stream signal intensity profiles through  $M_c = 0.79$  side view images for (a) the product formation method and (b) the passive scalar method.

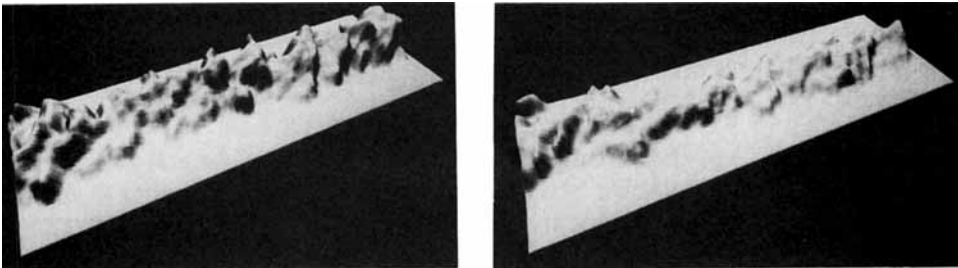


FIGURE 37. Perspective views of  $M_c = 0.79$  product formation side view images ( $x = 18-33$  cm).

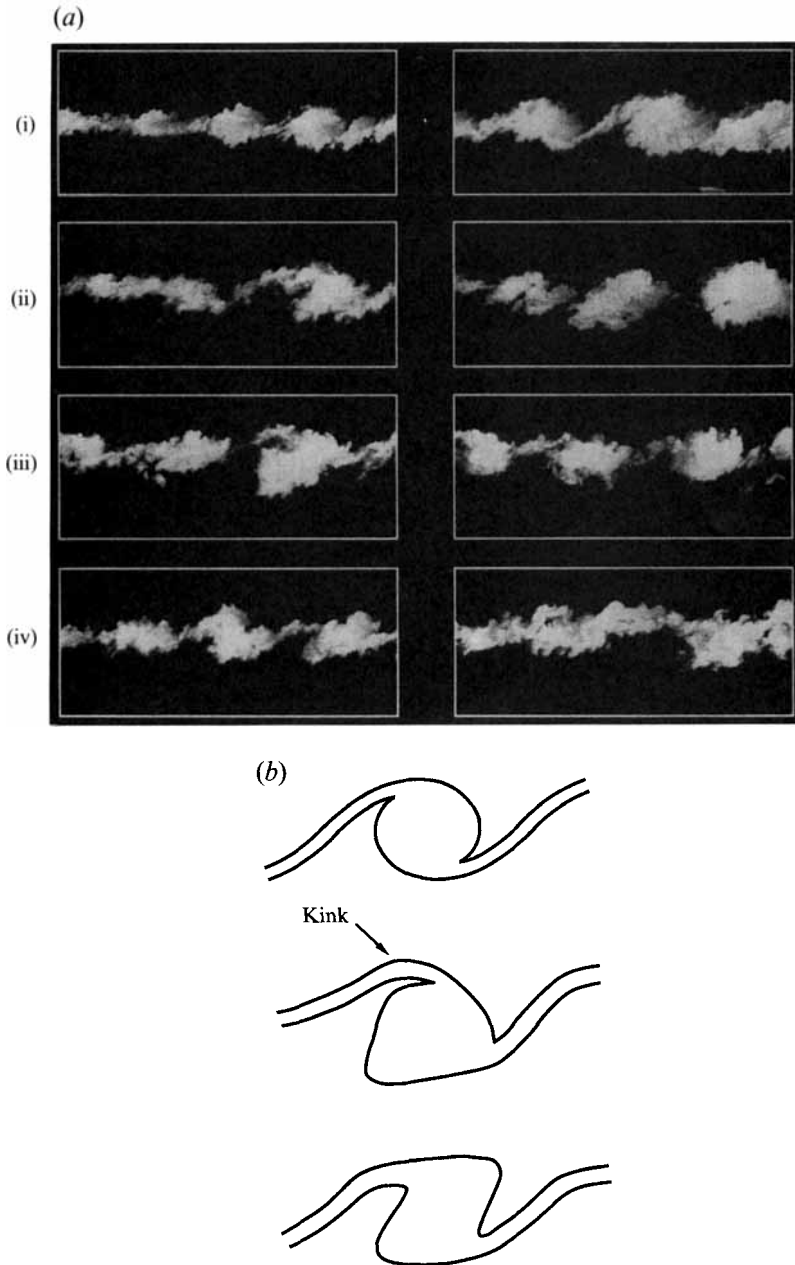


FIGURE 38. (a) Select images comparing roller structure at different convective Mach numbers: (i)  $M_c = 0.28$ , (ii)  $M_c = 0.42$ , (iii)  $M_c = 0.50$ , (iv)  $M_c = 0.62$ . (b) Schematic diagram showing roller structure: (top) low compressibility (middle, bottom) higher compressibility structures that exhibit polygonal appearance and a kink in the braid region.

schematically in figure 38(b). In addition to the change in the shape of the structure cores, the braid regions develop a ‘kink’ which is particularly noticeable at  $M_c = 0.5$  and  $0.62$ , but is not observed at  $M_c = 0.28$ . The reason for this change in the rollers is not known, and does not appear to have been predicted by linear stability theory or direct numerical simulations.

The changes from two- to three-dimensionality are in general agreement with the imaging results of Messersmith *et al.* (1991) and Elliott *et al.* (1993), where a decrease in organization of the layer was found with increasing convective Mach number. The present results also show general agreement with the static pressure space-time correlation results of Samimy *et al.* (1992) where the higher convective Mach number case was characterized by smaller spanwise correlation lengths. Furthermore, the  $M_c = 0.7$  visualizations of Fourquette *et al.* (1990), who used the condensation of water vapour in the product formation mode, also exhibit strong similarities with the side view images of the  $M_c = 0.62$  case.

This trend of increasing three-dimensionality was predicted using linear stability theory, and in the numerical simulations of Sandham & Reynolds (1991). The hairpin-type vortical structures found by Sandham & Reynolds, however, are not readily apparent from the present visualizations. The reason for this may be: (i) that the structures do not exist in real flows, (ii) that we are not visualizing them with the proper technique, or (iii) that the structures exist but so do many other modes which render any individual mode indistinguishable. It is not known which of the above explanations is correct but the simulations of Chen (1991) show that while the vortical structures are organized, the passive scalar field can appear disorganized. This is because the passive scalar field is affected by both recent and past vortical motions. The third reason also has merit however, as linear stability theory predicts that at the highest convective Mach numbers of this study, many oblique waves, of differing angles, are approximately equally amplified. Given that supersonic wind tunnels experience significant acoustic perturbations, this may result in a complex set of interacting instability modes. We should note that there is some disagreement on this issue since both the studies of Samimy *et al.* (1992) and Elliott *et al.* (1993) report evidence of structures that are similar to those simulated by Sandham & Reynolds (1991).

It should be emphasized that we do not believe that the observed changes from two- to three-dimensionality result from a Reynolds number effect. One reason for this is that since the Reynolds number varies by a factor of three from  $x = 15$  to 45 cm, Reynolds number effects would appear as a change in structure from the beginning to the end of the test section. This is not observed in any of the visualizations, however, since the character of the layer appears the same in all regions of the flow at a given Mach number. Furthermore, the Reynolds numbers are nearly the same for the  $M_c = 0.28$  case at  $x = 45$  cm and the  $M_c = 0.62$  case at  $x = 15$  cm, but the turbulent structure at those locations is completely different.

In addition to the observed transition from two- to three-dimensionality, several generalizations can be made regarding mixing and entrainment in the compressible layer. It was previously mentioned that at  $M_c = 0.28$  the structure core concentration is streamwise sloped and cross-stream uniform, which is consistent with a layer that is dominated by two-dimensional rollers. At  $M_c = 0.62$  and 0.79, however, streamwise profiles suggest that the structures are less often streamwise sloped, and the cross-stream profiles indicate that the structures are less uniform in the cross-stream direction than the lower convective Mach number cases. In particular it was noted that many of the structures exhibited profiles which were cross-stream sloped and even two-levelled, suggesting that the mixing occurs in steps across the layer. The perspective views show, however, that there are particular structures where a profile would appear to be two-levelled, but this is due to the overlap of two closely spaced structures. These closely spaced structures are possibly streamwise (or oblique) vortices, that are inclined from the  $x$ -axis. If this is so, then in the regions where the vortices are overlapping, the entrainment would occur in steps, with each vortex preferentially entraining fluid from

the side to which it is closest. The end views of figures 27 and 34 provide some evidence for this, because they can appear both highly convoluted, and seem to contain two separate regions of mixed fluid (these characteristics are particularly apparent at  $M_c = 0.79$ , for example, figure 34*b* (right)). Although speculative, this view is in general agreement with the direct numerical simulations of Sandham & Reynolds (1991) and Chen (1991), where in some regions two streamwise vortices of opposite sign are located such that one resides on top of the other.

Observation of the full ensemble of images suggests that the cross-stream sloped structures are a more dominant feature of the compressible layer than are the overlapping structures. It is also apparent that the cross-stream slopes are consistent with the observation that the original side view images (such as figure 32) appear to have a ‘fuzzy’ (small gradient) top interface, and a ‘sharp’ (large gradient) bottom interface. Although not as apparent as at  $M_c = 0.79$ , this same characteristic is also found at  $M_c = 0.62$ , but not at  $M_c = 0.28$  where both the top and bottom sides exhibit a sharp interface. The fuzzy high-speed side interface is consistent with the hot-wire measurements of Bonnet *et al.* (1993) who found that the mass flux fluctuations on the high-speed side of the layer were lower than at the low-speed side interface. It is also of note that the suppression of the fluctuations on the high-speed interface might be a direct result of the eddy convection velocity which is biased towards the velocity of the high-speed stream (Papamoschou 1991; Fourchette *et al.* 1990; McIntyre & Settles 1991; Hall *et al.* 1991*a*). Such a velocity bias results in structures which feel less shear on the high-speed interface, with a resulting decrease in the fluctuations on the high-speed side.

## 5. Experimental results: PLIF

This section presents PLIF visualizations and statistical results extracted from the images. A detailed discussion of the results follows in §6.

### 5.1. PLIF imaging: $M_c = 0.28$

Two single-shot corrected and smoothed images for the  $M_c = 0.28$  case are shown in figure 39. The images have been corrected for laser sheet non-uniformity and laser beam absorption, and were low pass filtered to improve the SNR (see §5.3.1). The NO was seeded into the low-speed stream, the flow is from left to right and  $x = 28\text{--}33$  cm. It should be emphasized that these images are quantitative representations of the instantaneous mixture fraction field. The images reveal a similar structure to that found using the PLMS methods, where large rollers dominate the flow field. As with the PLMS, however, not all of the images appear as rollers. Of particular note in these images are the ‘tongues’ of pure high- or low-speed fluid which sometimes penetrate well into the layer.

In figure 40, perspective views of the side view images are shown. The orientation of the axes is the same as in figure 16(*a*), where the point of view is from the high-speed side looking towards the low-speed side. The flow is therefore from right to left and the low-speed side, whose signal intensities have been mapped into height, is at the top. In this figure, the slopes discussed previously are shown very dramatically to extend from the lowest to the highest signal levels. Furthermore, the large gradients of the braid regions between the structures are rendered as very steep cliffs. The slopes are further seen to be fairly uniform in the cross-stream direction as was also found with the PLMS signals. As shown in figure 40(*a*), this cross-stream uniformity results in the mixed fluid being separated from each free stream by a relatively steep gradient.

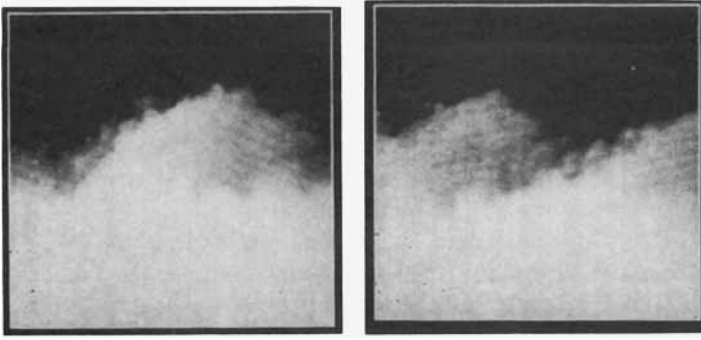
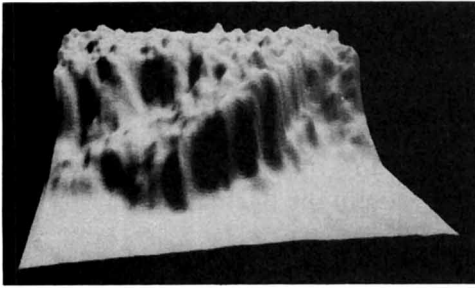


FIGURE 39. Side view PLIF images,  $M_c = 0.28$ ,  $x = 28\text{--}33$  cm and  $z = 0$  cm. The flow direction is from left to right.

(a)



(b)

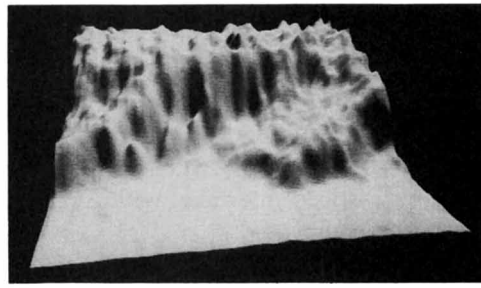


FIGURE 40. Perspective views of the side view PLIF images at  $M_c = 0.28$ .

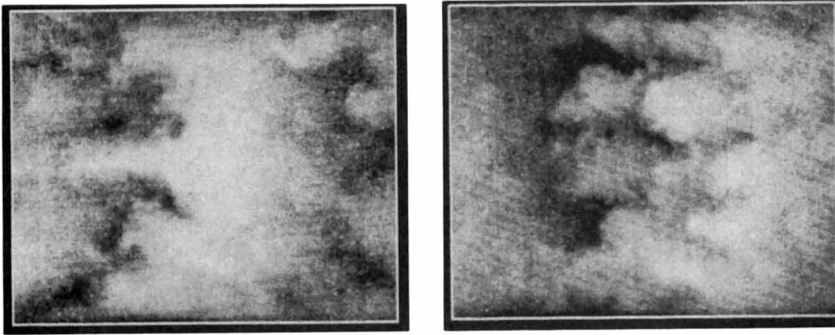


FIGURE 41. Plan view PLIF images,  $M_c = 0.28$ ,  $x = 28\text{--}33$  cm,  $z = -2.5\text{--}2.5$  cm and  $y = 0$  cm. The flow is from left to right.

Figure 40 also shows that the structure cores exhibit a large variation in mixture fraction. Figure 40(b) also shows that the slopes are not restricted to the streamwise direction only, as the core is both streamwise and cross-stream sloped.

In addition to side views, plan view images were taken at  $M_c = 0.28$ . These images cover the region from  $x = 28\text{--}33$  cm (about 1/3 that of the PLMS methods) with a width of 5 cm. The width of the image is the same as with the PLMS methods and the sheet was located at  $y = 0$  cm. Two independent images are shown in figure 41 which show the spanwise bands connected by streamwise braid structures as found with the passive scalar PLMS images of figure 12. A comparison of figures 41 and 12 shows that the streamwise structures appear to be oriented in opposite directions, resulting from

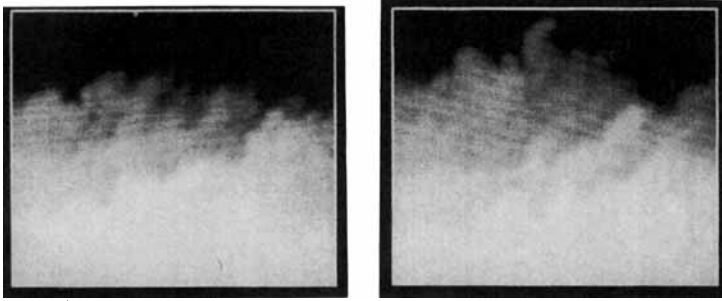


FIGURE 42. Side view PLIF images,  $M_c = 0.62$ ,  $x = 26\text{--}31$  cm and  $z = 0$  cm.

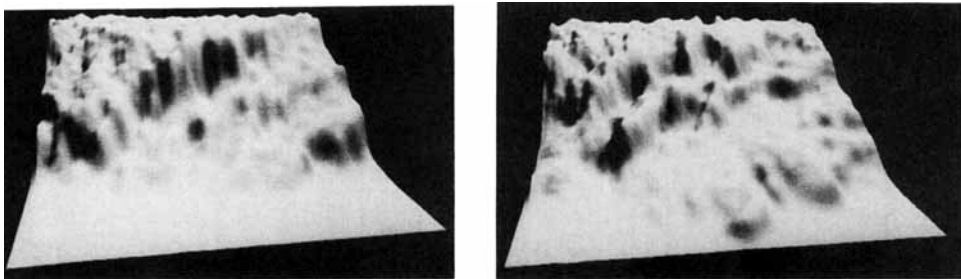


FIGURE 43. Perspective views of the side view PLIF images at  $M_c = 0.62$ .

the seeding of opposite free streams in the two cases. In general, it is seen that these quantitative PLIF images provide clear confirmation of the trends observed using the PLMS technique.

### 5.2. PLIF imaging: $M_c = 0.62$

In figure 42, two single-shot corrected and smoothed images for the  $M_c = 0.62$  case are shown. The field of view is also 5 cm and extends from  $x = 26$  to 31 cm, and the same amount of smoothing was performed on these images as with the  $M_c = 0.28$  case. The SNR for this case was about 40% higher than at  $M_c = 0.28$ , owing to the higher seeding levels used. These images reveal a structure which appears quite different from the lower convective Mach number case. For example, although large-scale structures are still present (as was seen with the PLMS images), they do not appear as roller-like. This is evidenced by the absence of large tongues of pure fluid penetrating deep into the layer.

Perspective views of these images are shown in figure 43. The viewing direction is the same as for figure 40, where the point of view is on the high-speed side looking towards the low-speed side. These perspective views provide a much clearer picture of the mixture fraction field than the images of figure 42, and reveal clear differences from the lower Mach number case. In agreement with the fog images, this case is dominated by structures that have mixture fraction fields which are sloped in the cross-stream rather than streamwise direction.

As was suggested by the profiles through the fog side views, the images of figure 43 show the two-levels of mixed fluid which are separated from each other by relatively steep gradients. In the first image, these two regions exist as parallel streamwise sloped structures, which are much thinner than the sloped structures at the lower convective Mach number. For the other image, the two regions are not as sloped but are separated by an even steeper gradient. This image also shows that most of the mixed fluid of this structure exists in the large diffuse region which is dominated by high-speed fluid. As

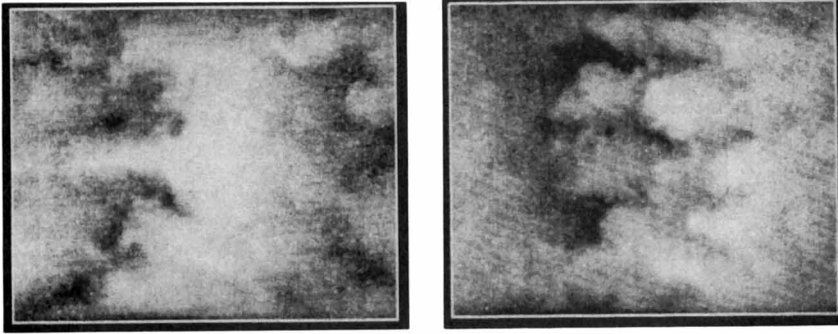


FIGURE 44. Plan view PLIF images,  $M_c = 0.62$ ,  $x = 26\text{--}31$  cm,  $z = -2.5\text{--}2.5$  cm and  $y = 0$  cm.

was discussed previously, the two-levelled structures appear to be caused by slanted and overlapping structures which may entrain fluid preferentially from the free stream to which they are closest. Furthermore, the large diffuse regions that are dominated by high-speed fluid are consistent with the fog visualizations that indicated a ‘fuzzy’ (i.e. weak gradient) high-speed interface.

Plan views for the  $M_c = 0.62$  case are shown in figure 44, where  $x = 26\text{--}31$  cm,  $z = -2.5\text{--}2.5$  cm,  $y = 0$  cm, and the flow is from left to right. These images reveal the same highly three-dimensional structure observed in the PLMS plan views.

### 5.3. PLIF statistical results

#### 5.3.1. Defining equations

Various statistical quantities for both convective Mach number cases were computed using the full sets of 120 images. The statistics were computed by treating each row of an image as a record of time series data. To take advantage of the higher SNR near the centre of the images (near the peak of the sheet profile) only about 40% (about 2 cm) of the image area was used. At this location, the layer grows by less than 5% over the width of the processing region, which was considered small enough so as not to influence the results when treating the data as a time series. The total amount of data considered corresponded to the passage of about 80 large-scale structures and about 24000 data points per  $y$ -location, and is consistent with previous studies where approximately 100 structures were averaged (Mungal & Dimotakis 1984; Koochesfahani & Dimotakis 1986). The images were low pass filtered to approximately double the SNR to a value of about 20. The filtering resulted in a significant loss in resolution, such that  $L/\lambda_B = 500\text{--}800$ . This is worse than all of the measurements of table 1, except that of Koochesfahani & Dimotakis (1986). We caution that although the signal grey scales are interpreted here as ‘mixed’ fluid, the actual extent of molecular mixing cannot be determined at the sub-resolution scale. For the relative resolution of the present measurements, the true amount of mixed fluid may be overestimated by as much as a factor of two (Koochesfahani & Dimotakis 1986).

For the statistical computations, the intensity data were converted to high-speed fluid mixture fraction using equation (3). The mixture fraction,  $\xi$ , is defined such that pure high-speed fluid is unity and pure low-speed fluid is zero.

The normalized cross-stream direction,  $\eta$ , is designated

$$\eta = (y - y_{0.5})/\delta_1, \quad (5)$$

where  $y_{0.5}$  is the cross-stream location where the mean mixture fraction equals 0.5, and  $\delta_1$  is the thickness corresponding to the 1% and 99% mean mixture fraction points.

The statistical quantities presented below are profiles of the mean mixture fraction and the root-mean-square (RMS) fluctuations, which are calculated from the PDFs of mixture fraction. The PDF of mixture fraction,  $P(\xi, \eta)$ , at a given  $\eta$ -location, is calculated for each row of an image by compiling a histogram of the range of mixture fractions. Each PDF is normalized such that

$$\int_{-\infty}^{\infty} P(\xi, \eta) d\xi = 1. \quad (6)$$

The integration is between plus and minus infinity rather than zero and unity because noise creates a distribution of values around the pure state. The mean mixture fraction,  $\bar{\xi}$ , and RMS fluctuations,  $(\bar{\xi}'^2)^{1/2}$  are calculated from the relations for the mean and the variance:

$$\bar{\xi} = \int_{-\infty}^{\infty} \xi P(\xi, \eta) d\xi, \quad (7)$$

$$\bar{\xi}'^2 = \int_{-\infty}^{\infty} (\xi - \bar{\xi})^2 P(\xi, \eta) d\xi. \quad (8)$$

### 5.3.2. $M_c = 0.28$

Figure 45(a) shows the mean and RMS fluctuation profiles of mixture fraction for the  $M_c = 0.28$  case. The mean profiles are largely insensitive to resolution (Koochesfahani & Dimotakis 1986) and also to SNR as long as the statistics have converged. Figure 45(a) shows that the mean profile exhibits a single inflection point, in agreement with the results of Batt (1977) and Sunyach & Mathieu (1969). Several investigators, however, have measured mean profiles with a characteristic 'S' shape or triple inflection point (table 1), as will be discussed further in §6.

The RMS fluctuations do not go to zero at either free stream owing to the shot noise of the measurement. Since shot noise is proportional to the square root of the signal, the noise is highest in the low-speed free stream. If this noise offset were removed, the profile would appear more top-hat shaped in agreement with the results Fiedler (1974), Batt (1977), and Konrad (1977), where either double-peaked or top-hat profiles were measured. Furthermore, the peak fluctuations are about 17% (about 2% of which is noise) whereas Konrad (1977), Fiedler (1974) and Batt (1977) found fluctuations levels of 40%, 30% and 20%, respectively.

The PDFs of mixture fraction are shown in figure 45(b), and show that the most probable mixture fraction marches across the layer. This marching behaviour is in agreement with the incompressible results of Batt (1977) and Karasso & Mungal (1992) and the supersonic mixing layer measurements of Dutton *et al.* (1990) and Clemens & Paul (1993). The marching PDFs do not agree, however, with the results of Konrad (1977) and Koochesfahani & Dimotakis (1986) and the pre-mixing transition measurements of Masutani & Bowman (1986). Mungal & Dimotakis (1984) suggest that marching PDFs, such as that of Batt (1977), are an artifact resulting from insufficient resolution. It is seen in table 1, however, that there does not appear to be an obvious relationship between relative resolution and the shape of the PDFs. In fact, both the best and worst resolution experiments exhibit non-marching PDFs.

### 5.3.3. $M_c = 0.62$

Figure 46(a) shows the mean and RMS fluctuation profiles for the  $M_c = 0.62$  case. As was found at  $M_c = 0.28$ , the mean profile exhibits a single inflection point. The RMS fluctuations profile exhibits a shape similar to that at  $M_c = 0.28$ , but only attains a maximum value of 13% (about 2% of which is noise).

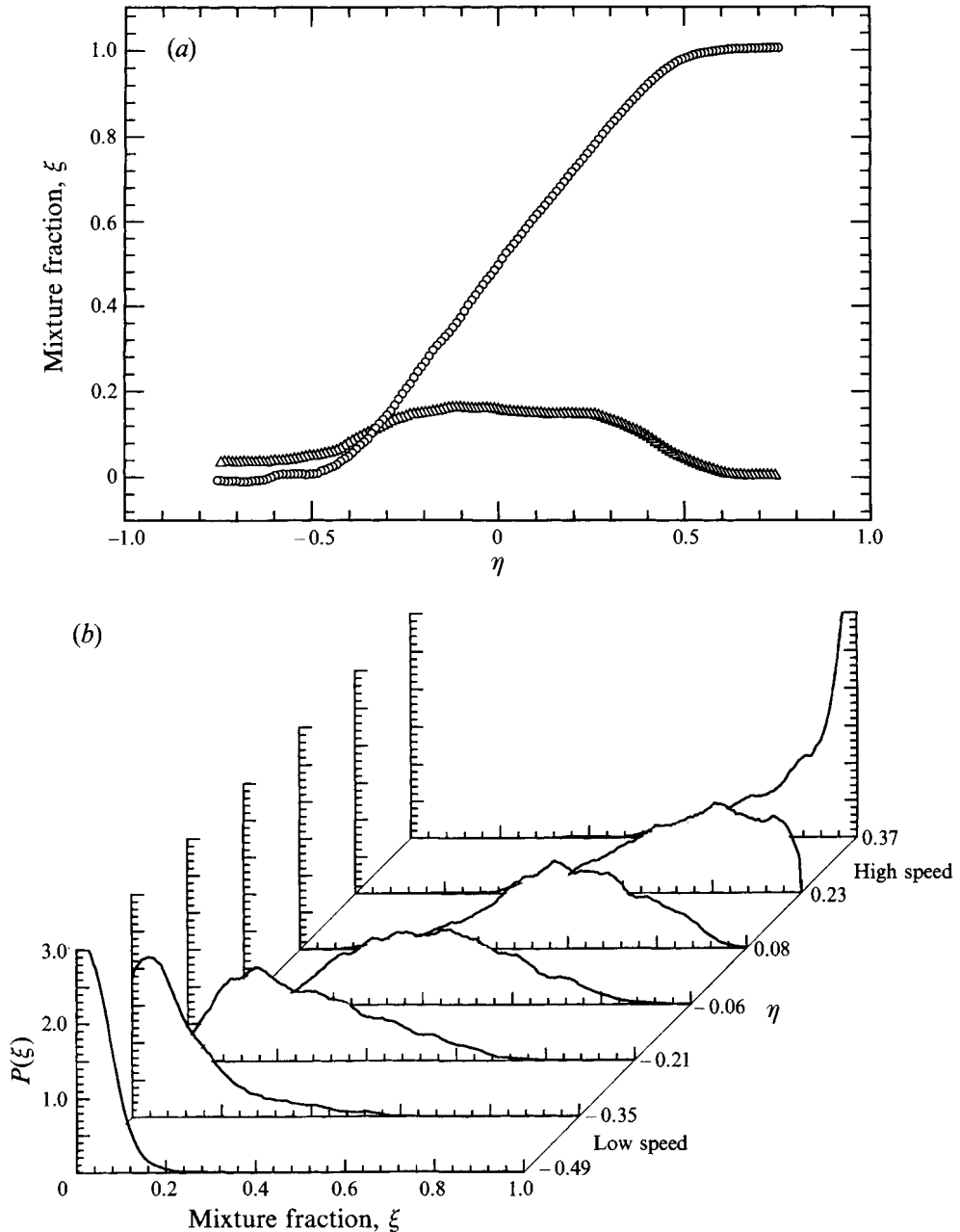


FIGURE 45. Mixture fraction statistics for  $M_c = 0.28$ : (a) mean (O) and RMS ( $\Delta$ ) fluctuations, (b) PDFs for several cross-stream locations.

Figure 46(b) shows that the PDFs of mixture fraction also exhibit marching behaviour. Compared to figure 45(b), however, the PDF at each location has a higher peak and a smaller width, suggesting that for the  $M_c = 0.62$  case a smaller range of mixture fractions are present at a given location. Several of the PDFs in figure 46(b) also appear to be flat topped (or even double-humped), which may be related to the multi-levelled structures of figure 43.

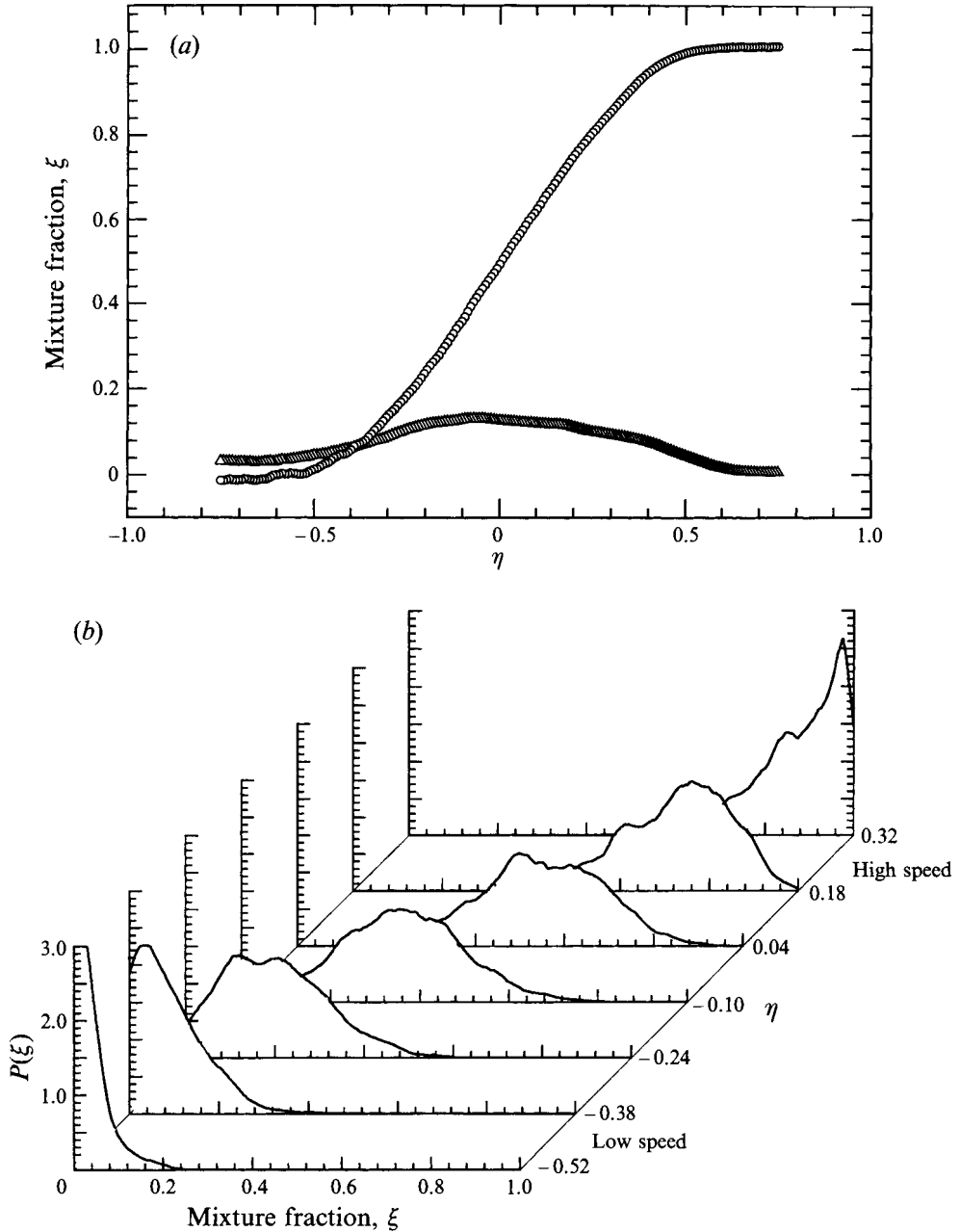


FIGURE 46. Mixture fraction statistics for  $M_c = 0.62$ : (a) mean ( $\circ$ ) and RMS ( $\triangle$ ) fluctuations, (b) PDFs for several cross-stream locations.

## 6. Discussion

In figure 47(a), the mean profiles at  $M_c = 0.28$  and  $0.62$  are shown plotted together. The profiles are now seen to be nearly identical. This is not surprising, however, when one considers that the mean is the first moment of the PDF, thus a single inflection point is a consequence of PDFs that are both marching and symmetric about the  $\eta$ -axis. A similar argument can be made for the triple inflection point, which is a natural consequence of non-marching PDFs. This is seen in table 1, where there is a good

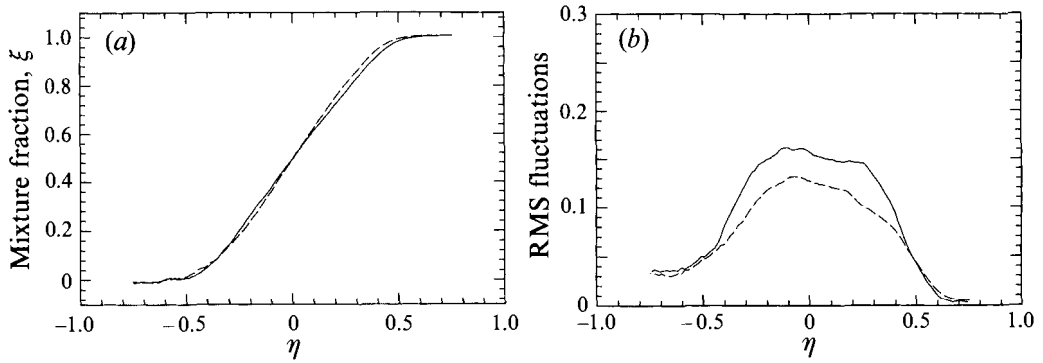


FIGURE 47. Comparison of profiles at  $M_c = 0.28$  (—) and  $M_c = 0.62$  (---): (a) mean, (b) RMS fluctuations.

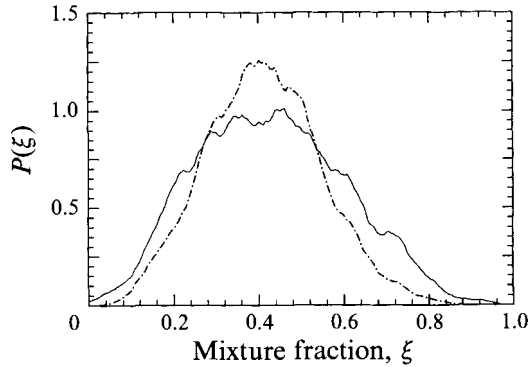


FIGURE 48. Comparison of PDFs of mixture fraction for  $M_c = 0.28$  (—) and  $M_c = 0.62$  (---) for  $\eta \approx 0$ .

correlation between the triple inflection point and non-marching PDFs. From the clear triple inflection point in the mean profiles of Fiedler (1974), we would expect his PDFs (if presented) to be non-marching.

Fiedler (1974) argued that triple inflection point profiles result from layers that are dominated by coherent structures with compositions that are cross-stream uniform and streamwise sloped. Although, in this study at  $M_c = 0.28$ , the trend of cross-stream uniform and streamwise sloped structures was observed, there was sufficient variation in the composition of the structures to remove any indication of a triple inflection point.

The RMS fluctuations for the two cases are compared in figure 47(b), and show the fluctuations at  $M_c = 0.28$  are about 15% greater than those at  $M_c = 0.62$ . This is in agreement with the results of Dutton *et al.* (1990) and Clemens & Paul (1993) for a similar convective Mach number range. The hot-wire measurements of Bonnet *et al.* (1993) indicate that at moderate compressibility mass flux fluctuations are suppressed to a larger extent on the high-speed edge of the layer. This also appears to be the case for the mixture fraction fluctuations of figure 47(b) at  $M_c = 0.62$ .

The narrower PDFs for the higher convective Mach number case were mentioned above and this is more clearly seen in figure 48 which shows PDFs at  $\eta \approx 0$  for the two cases. This figure shows that at  $M_c = 0.62$ , the PDF is somewhat narrower than at  $M_c = 0.28$ . A Gaussian profile was fit to each curve and showed that the  $e^{-1}$  width is about

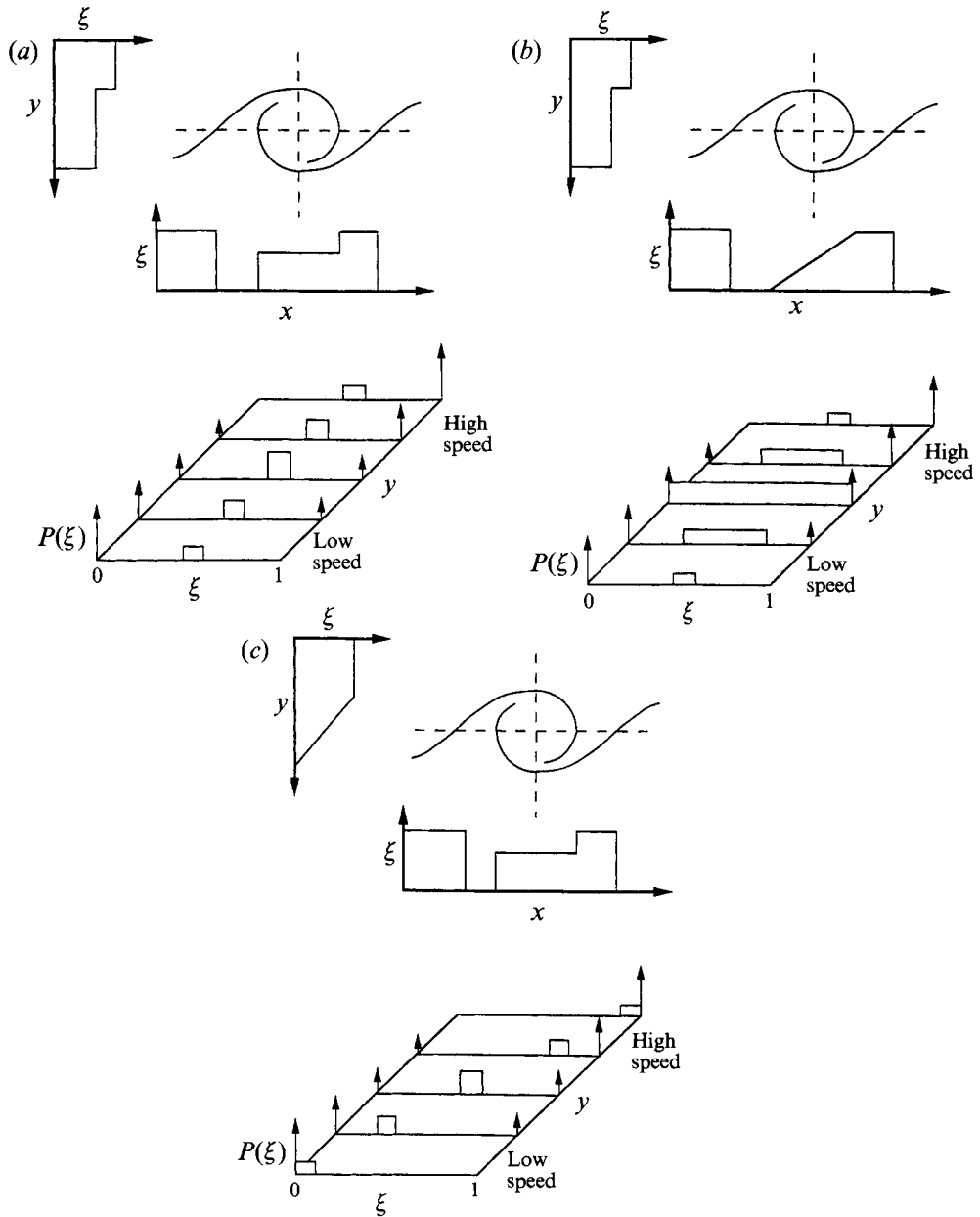


FIGURE 49. Model PDFs: streamwise and cross-stream profiles are shown at the top, and the model PDFs are shown at the bottom: (a) uniform core, (b) streamwise sloped and cross-stream uniform, (c) streamwise uniform and cross-stream sloped.

20% larger at  $M_c = 0.28$ . Broader PDFs imply that a larger range of mixture fraction values is present at a given location. These broad PDFs are responsible for the larger RMS fluctuations found at the lower convective Mach number.

The obvious issue that arises is what types of turbulent structures are responsible for the resulting PDFs. As a means of understanding this, we consider three model turbulent structures. The first, figure 49(a), is similar to that modelled by Broadwell & Breidenthal (1982) and is uniform in both the streamwise and the cross-stream

directions. For this type of structure the PDFs would exhibit a preferred mixture fraction at all transverse locations across the layer. If the typical structure is sloped in the streamwise direction, yet uniform in the cross-stream direction (figure 49*b*), as was suggested by Fiedler (1974), then the PDFs also exhibit a preferred mixture fraction which is invariant with the transverse location. The PDFs are different from figure 49*a*), however, because the slope results in a much broader range of mixture fractions populating a given location. The final model, figure 49*c*), is that of a structure which resembles the mean because it is uniform in the streamwise direction and sloped in the cross-stream direction. In this case, the PDFs appear as a series of marching delta functions which reflect the small range of mixture fractions that are present at each cross-stream location.

The model PDFs suggest that the mixing layer at  $M_c = 0.28$  may exhibit characteristics of both the streamwise and cross-stream sloped models, because the PDFs are both broadly distributed and marching. Some evidence of this is provided by the perspective views of figure 40 which exhibit both types of sloped structure. For the  $M_c = 0.62$  case, the narrower PDFs are consistent with the cross-stream sloped model, as are the perspective views of figure 43. This suggests that the compressible layer, unlike its incompressible counterpart, is composed of turbulent structures whose instantaneous mixture fraction profiles more closely resemble the mean profile. This view is consistent with the 'sonic eddy' model developed by Breidenthal (1992), which predicts that compressibility acts to reduce the eddy lengthscales which are responsible for entrainment. The entrainment by smaller-scale eddies results in instantaneous cross-stream profiles which are similar to the mean profile.

Unfortunately, owing to the limited resolution of the measurement, we cannot make a definitive statement as to the extent of molecular mixing. This was shown by Koochesfahani & Dimotakis (1986) in incompressible mixing layers and by Clemens & Paul (1993) in compressible axisymmetric mixing layers, where under-resolved passive scalar measurements were shown to significantly overestimate the amount of mixed fluid in the layer. Since under-resolved passive scalar measurements cannot be trusted to provide information on molecular mixing, it is necessary to rely on measurements which are insensitive to limited resolution. Hall *et al.* (1991*b*) used fast chemical reactions and found that the fraction of mixed fluid in the layer is about 30% greater at  $M_c = 0.51$  than at  $M_c = 0.91$ . In axisymmetric mixing layers, Clemens & Paul (1993) found little difference in the fraction of mixed fluid at convective Mach numbers of 0.35 and 0.82. The reason for the difference in the two measurements is not known, but it should be safe to conclude that compressibility does not greatly increase the fraction of mixed fluid.

For the present results, the observed changes in the entrainment with compressibility such as increased three-dimensionality, closely spaced and cross-stream sloped structures and smaller scalar fluctuations, are probably more consistent with a compressible mixing layer which has a larger fraction of mixed fluid. If we assume that these effects increase the amount of stirring at the large scales, then we might expect this to facilitate the mixing process (i.e. inter-diffusion). The mixing measurements mentioned above, however, indicate that this is not the case, or is at most a very small effect. This leads to the possibility that compressibility increases the amount of stirred fluid at the larger scales, while somehow reducing stirring and/or diffusion at the smaller scales. This, of course, is largely conjecture, but it does suggest the need for continued research into this very complex problem.

Even though the exact nature of the mixing process at the small scales is not well understood, the changes in the structure and entrainment process that we have

documented have strong implications for the understanding of reacting mixing layers. In particular, we have seen that the breakdown of the two-dimensional structure results in a mixture fraction field which differs significantly from what is found under incompressible conditions. Since in a reacting situation the mixture fraction field will determine the local stoichiometry and temperature, the mode of burning can be expected to be significantly modified. This indeed appears to be the case as suggested by the reacting mixing layer results of Miller *et al.* (1993) who studied  $H_2$ /vitiated air supersonic mixing layers at moderate levels of heat release, and cite similarities in the structure of the fuel and OH fields to that found in the present cold flow studies.

## 7. Conclusions

Studies of the large-scale structure, entrainment motions, and mixture fraction fluctuations were made at a range of convective Mach numbers. Flow visualizations using planar laser Mie scattering from condensed alcohol droplets reveal a mixing layer that is dominated by spanwise rollers at  $M_c = 0.28$  and  $0.42$ , but much more three-dimensional and apparently unorganized structures at  $M_c = 0.62$  and  $0.79$ . There is also some evidence for increased streamwise structure at the highest convective Mach numbers. The convective Mach number of  $0.50$  appears to be transitional as both rollers and the more unorganized structures seen at higher  $M_c$  are observed. A change was also seen in the character of the structure core and braid regions of the rollers with increasing compressibility. The shape of the structure cores transition from elliptical to polygonal, and the braids developed a characteristic 'kink'. Observations of entrainment of fluid into the mixing layer suggest that at low  $M_c$  the mixture fraction field is sloped in the streamwise direction, but more uniform in the cross-stream direction. At  $M_c = 0.62$  and  $0.79$ , the mixture fraction field was often found to be sloped in the cross-stream direction and sometimes showed two distinct regions of mixing due to closely spaced overlapping structures. The exact vortical structure which causes these overlapping structures could not readily be identified, but the likely cause is closely spaced streamwise vortices.

Quantitative images of the mixture fraction field were obtained using planar laser-induced fluorescence of seeded nitric oxide at convective Mach numbers of  $0.28$  and  $0.62$ . These images provided validation of the trends seen in the Mie scattering visualizations and provided an opportunity to quantitatively investigate the mixture fraction field. Mixture fraction statistical quantities were computed, such as the mean, RMS fluctuations and PDFs. The mean profiles are similar for both cases but the RMS fluctuations are about 15% smaller at  $M_c = 0.62$ . The fluctuations are particularly suppressed on the high-speed edge of the layer. The PDFs for both cases exhibit a peak in mixture fraction which marches across the layer, but individual PDFs are typically broader at  $M_c = 0.28$ . These results are consistent with the qualitative observations at  $M_c = 0.62$  of fewer pure fluid intrusions into the layer and of weaker scalar gradients on the high-speed edge of the layer. The present results also suggest that compressibility increases the amount of stirring at the large scales which might help the layer to become better mixed. Previous mixing measurements, however, suggest that this is not the case, as compressibility appears to reduce or have little effect on the efficiency of molecular mixing.

This work was sponsored by the US AFOSR, Aerospace Sciences Directorate, J. Tishkoff technical monitor, and the NASA Ames/Stanford University Center for Turbulence Research. We gratefully acknowledge the help of Mr M. F. Miller in

construction of the facility. The PLIF diagnostics were also developed under the sponsorship of the AFOSR by Professor R. K. Hanson. The expert help of Dr P. H. Paul and R. K. Hanson in conducting these measurements is gratefully acknowledged.

## REFERENCES

- BATT, R. G. 1977 Turbulent mixing of passive and chemically reacting species in a low-speed shear layer. *J. Fluid Mech.* **82**, 53–95.
- BERNAL, L. P. & ROSHKO, A. 1986 Streamwise vortex structure in plane mixing layers. *J. Fluid Mech.* **170**, 499–525.
- BIRCH, S. F. & EGGERS, J. M. 1972 A critical review of the experimental data for developed free turbulent shear layers. *NASA SP-321*, pp. 11–40.
- BOGDANOFF, D. W. 1983 Compressibility effects in turbulent shear layers. *AIAA J.* **21**, 926–927.
- BONNET, J. P., DEBISSCHOP, J. R. & CHAMBRES, O. 1993 Experimental studies of the turbulent structure of supersonic mixing layers. *AIAA Paper* 93-0217.
- BREIDENTHAL, R. 1981 Structure in turbulent mixing layers and wakes using a chemical reaction. *J. Fluid Mech.* **109**, 1–24.
- BREIDENTHAL, R. 1992 Sonic eddy – A model for compressible turbulence. *AIAA J.* **30**, 101–104.
- BROADWELL, J. E. & BREIDENTHAL, R. E. 1982 A simple model of mixing and chemical reaction in a turbulent shear layer. *J. Fluid Mech.* **125**, 397–410.
- BROWAND, F. K. & LATIGO, B. O. 1979 Growth of the two-dimensional mixing layer from a turbulent and nonturbulent boundary layer. *Phys. Fluids* **22**, 1011–1019.
- BROWAND, F. K. & TROUTT, T. R. 1985 The turbulent mixing layer: Geometry of the large vortices. *J. Fluid Mech.* **158**, 489–509.
- BROWN, G. L. & ROSHKO, A. 1974 On density effects and large structure in turbulent mixing layers. *J. Fluid Mech.* **64**, 775–816.
- CHANDRSUDA, C., MEHTA, R. D., WEIR, A. D. & BRADSHAW, P. 1978 Effect of free-stream turbulence on large structure in turbulent mixing layers. *J. Fluid Mech.* **85**, 693–704.
- CHEN, J. H. 1991 The effect of compressibility on conserved scalar entrainment in a plane free shear. *Eighth Symp. on Turbulent Shear Flows, Munich, Germany*.
- CHINZEI, N., MASUYA, G., KOMURO, T., MURAKAMI, A. & KUDOU, K. 1986 Spreading of two-stream supersonic mixing layers. *Phys. Fluids* **29**, 1345–1347.
- CLEMENS, N. T. 1991 An experimental investigation of scalar mixing in supersonic turbulent shear layers. PhD thesis, High Temperature Gas Dynamics Laboratory, Mechanical Engineering Department, Stanford University.
- CLEMENS, N. T. & MUNGAL, M. G. 1991 A planar Mie scattering technique for visualizing supersonic mixing flows. *Expts Fluids* **11**, 175–185.
- CLEMENS, N. T. & MUNGAL, M. G. 1992a Two- and three-dimensional effects in the supersonic mixing layer. *AIAA J.* **30**, 973–981.
- CLEMENS, N. T. & MUNGAL, M. G. 1992b Effects of sidewall disturbances on the supersonic mixing layer. *J. Propulsion Power* **8**, 249–251.
- CLEMENS, N. T. & PAUL, P. H. 1993 Scalar measurements in compressible axisymmetric mixing layers. *AIAA Paper* 93-0220.
- CLEMENS, N. T., PAUL, P. H., MUNGAL, M. G. & HANSON, R. K. 1991 Scalar mixing in the supersonic shear layer. *AIAA Paper* 91-1720.
- CRAWFORD, M. E. & KAYS, W. M. 1976 STAN5-A program for numerical computation of two-dimensional internal and external boundary layer flows. *NASA CR-2742*.
- DOWLING, D. R. & DIMOTAKIS, P. E. 1990 Similarity of the concentration field of gas-phase turbulent jets. *J. Fluid Mech.* **218**, 109–142.
- DUTTON, J. C., BURR, R. F., GOEBEL, S. G. & MESSERSMITH, N. L. 1990 Compressibility and mixing in turbulent free shear layers. *Presented at the 12th Symposium on Turbulence, Sept. 24–26, Rolla, MO*, p. A21-1.
- ELLIOTT, G. S. & SAMIMY, M. 1990 Compressibility effects in free shear layers. *Phys. Fluids A* **2**, 1231–1240.

- ELLIOTT, G. S., SAMIMY, M. & ARNETTE, S. A. 1993 Study of compressible mixing layers with filtered Rayleigh scattering based visualizations. *AIAA J.* **30**, 2567–2569.
- FIEDLER, H. E. 1974 Transport of heat across a plane turbulent mixing layer. *Adv. Geophys.* **18**, 93–109.
- FOELSCH, K. 1946 A new method of designing two-dimensional laval nozzles for a parallel and uniform jet. *Rep. NA-46-235-2*. North American Aviation, Inc.
- FOURGUETTE, D. C., MUNGAL, M. G. & DIBBLE, R. W. 1990 Time evolution of the shear layer of a supersonic axisymmetric jet at matched conditions. *AIAA J.* **29**, 1123–1130.
- GOEBEL, S. G. & DUTTON, J. C. 1991 Experimental study of compressible turbulent mixing layers. *AIAA J.* **29**, 538–546.
- HALL, J. L., DIMOTAKIS, P. E. & ROSEMANN, H. 1991*a* Experiments in non-reacting compressible shear layers. *AIAA Paper* 91-0629.
- HALL, J. L., DIMOTAKIS, P. E. & ROSEMANN, H. 1991*b* Some measurements of molecular mixing in compressible turbulent shear layers. *AIAA Paper* 91-1719.
- HANSON, R. K., SEITZMAN, J. M. & PAUL, P. H. 1990 Planar laser-induced fluorescence imaging of combustion gases. *Appl. Phys. B* **50**, 441–454.
- IKAWA, H. & KUBOTA, T. 1975 Investigation of supersonic turbulent mixing layer with zero pressure gradient. *AIAA J.* **13**, 566–572.
- JACKSON, T. L. & GROSCH, C. E. 1989 Inviscid spatial stability of a compressible mixing layer. *J. Fluid Mech.* **208**, 609–637.
- KARASSO, P. S. & MUNGAL, M. G. 1992 LIF measurements of mixing in turbulent shear layers. *Sixth Intl Symp. on Applications of Laser Techniques to Fluid Mechanics, Lisbon, Portugal*.
- KONRAD, J. H. 1977 An experimental investigation of mixing in two-dimensional turbulent shear flows with applications to diffusion-limited chemical reactions. PhD thesis, California Institute of Technology.
- KOCHESFAHANI, M. M. & DIMOTAKIS, P. E. 1986 Mixing and chemical reactions in a turbulent liquid mixing layer. *J. Fluid Mech.* **170**, 83–112.
- MASUTANI, S. M. & BOWMAN, C. T. 1986 The structure of a chemically reacting plane mixing layer. *J. Fluid Mech.* **172**, 93–126.
- MAYDEW, R. C. & REED, J. F. 1963 Turbulent mixing of compressible free jets. *AIAA J.* **1**, 1443–1444.
- MCGREGOR, I. 1961 The vapor screen method of flow visualization. *J. Fluid Mech.* **11**, 481–511.
- MCINTYRE, S. S. & SETTLES, G. S. 1991 Optical experiments on axisymmetric compressible turbulent mixing layer. *AIAA Paper* 91-0623.
- MESSERSMITH, N. L. & DUTTON, J. C. 1992 An experimental investigation of organized structure and mixing in compressible turbulent free shear layers. *Rep. UILU-ENG 92-4002*. University of Illinois, Dept. of Mechanical and Industrial Engineering.
- MESSERSMITH, N. L., DUTTON, J. C. & KRIER, H. 1991 Experimental investigation of large scale structures in compressible mixing layers. *AIAA Paper* 91-0244.
- MILLER, M. F., ISLAND, T. C., SEITZMAN, J. M., BOWMAN, C. T., MUNGAL, M. G. & HANSON, R. K. 1993 Compressibility effects in a reacting mixing layer. *AIAA Paper* 93-1771.
- MUNGAL, M. G. & DIMOTAKIS, P. E. 1984 Mixing and combustion with low heat release in a turbulent shear layer. *J. Fluid Mech.* **148**, 349–382.
- MUNGAL, M. G. & FRIELER, C. E. 1988 The effects of Damkohler number in a turbulent shear layer. *Combust. Flame* **71**, 23–34.
- PAPAMOSCHOU, D. 1991 Structure of the compressible turbulent shear layer. *AIAA J.* **29**, 680–681.
- PAPAMOSCHOU, D. & ROSHKO, A. 1988 The compressible turbulent shear layer: an experimental study. *J. Fluid Mech.* **197**, 453–477.
- PAUL, P. H. 1991 The application of intensified array detectors to quantitative planar laser-induced fluorescence imaging. *AIAA Paper* 91-2315.
- PETULLO, S. P. & DOLLING, D. S. 1993 Large-scale structure orientation in a compressible turbulent shear layer. *AIAA Paper* 93-0545.
- RAGAB, S. A. & WU, J. L. 1989 Linear instabilities in two-dimensional compressible mixing layers. *Phys. Fluids A* **1**, 957–966.

- RAJAGOPALAN, S. & ANTONIA, R. A. 1981 Properties of the large structure in a slightly heated turbulent mixing layer of a plane jet. *J. Fluid Mech.* **105**, 261–281.
- SAMIMY, M. & LELE, S. K. 1991 Motion of particles with inertia in a compressible free shear layer. *Phys. Fluids A* **3**, 1915–1923.
- SAMIMY, M., REEDER, M. F. & ELLIOTT, G. S. 1992 Compressibility effects on large structures in free shear flows. *Phys. Fluids A* **4**, 1251–1258.
- SANDHAM, N. D. & REYNOLDS, W. C. 1991 Three-dimensional simulations of large-eddies in the compressible mixing layer. *J. Fluid Mech.* **224**, 133–158.
- SHAU, Y. R. & DOLLING, D. S. 1992 Exploratory study of turbulent structure of a compressible shear layer using fluctuating Pitot pressure measurements. *Exps Fluids* **12**, 293–306.
- SIRIEIX, M. & SOLIGNAC, J. L. 1966 Contribution a l'étude expérimentale de la coche de mélange turbulent isobare d'un écoulement supersonique. *AGARD CP* **4**, 242–270.
- SUNYACH, M. & MATHIEU, J. 1969 Mixing zone of a two-dimensional jet. *Intl J. Heat Mass Transfer* **12**, 1679–1697.
- WEGENER, P. P., CLUMPNER, J. A. & WU, B. J. C. 1972 Homogeneous nucleation and growth of ethanol drops in supersonic flow. *Phys. Fluids* **15**, 1869–1876.
- WYGNANSKI, I., OSTER, D., FIEDLER, H. & DZIOMBA, B. 1979 On the perseverance of a quasi-two-dimensional eddy-structure in a turbulent mixing layer. *J. Fluid Mech.* **93**, 325–335.
- ZHUANG, M., DIMOTAKIS, P. E. & KUBOTA, T. 1990 The effect of walls on a spatially growing supersonic shear layer. *Phys. Fluids A* **2**, 599–608.